Lari M. Koponen

Large thin overlapping coils, a novel approach for multichannel transcranial magnetic stimulation

School of Science

Thesis submitted for examination for the degree of Master of Science in Technology.
Espoo, 27th May, 2013

Thesis supervisor:

Academy Prof. Risto J. Ilmoniemi

Thesis advisor:

Dr. Jaakko O. Nieminen

Aalto University
School of Science

AALTO UNIVERSITY
SCHOOL OF SCIENCE

ABSTRACT OF THE
MASTER'S THESIS

Author: Lari M. Koponen

Title: Large thin overlapping coils, a novel approach for multichannel transcranial magnetic stimulation

Date: 27th May, 2013 Language: English Number of pages: 6+52

Department of Biomedical Engineering and Computational Science

Professorship: Biomedical Engineering Code: Tfy-99

Supervisor: Academy Prof. Risto J. Ilmoniemi

Advisor: Dr. Jaakko O. Nieminen

Transcranial magnetic stimulation (TMS) allows for studying the functionality of the brain. Present TMS devices have one or two separate stimulation coils. More stimulation coils would allow new types of stimulation sequences, and thus they could be used to reveal more about brain functionality. However, due to the dimensions of the existing TMS coils, having multiple separate coils is a very limited approach. Rather, the coils should be combined into a single multichannel (mTMS) device.

The purpose of this Thesis is to make mTMS more feasible. In order to realize this purpose, a new coil design paradigm is introduced which employs large thin overlapping coils. This paradigm requires a new coil design method and a new coil-former design method, which are developed and tested in this Thesis. This Thesis solves two problems that appear with existing mTMS designs and is a significant step towards successful mTMS.

Keywords: multichannel transcranial magnetic stimulation, TMS, mTMS, stimulation coil, coil design

AALTO-YLIOPISTO
PERUSTIETEIDEN KORKEAKOULU

DIPLOMITYÖN
TIIVISTELMÄ

Tekijä: Lari M. Koponen

Työn nimi: Suurikokoiset päällekkäiset kelat, uusi lähestymistapa monikanavaisen transkraniaalisen magneettistimulaatiolaitteen rakentamiseen

Päivämäärä: 27.5.2013 Kieli: Englanti Sivumäärä: 6+52

Lääketieteellisen tekniikan ja laskennallisen tieteen laitos

Professuuri: Lääketieteellinen tekniikka Koodi: Tfy-99

Valvoja: Akatemiaprofessori Risto J. Ilmoniemi

Ohjaaja: TkT Jaakko O. Nieminen

Transkraniaalinen magneettistimulaatio (TMS) mahdollistaa aivotoiminnan tutkimisen. Nykyisissä TMS-laitteissa on yleensä yksi tai joissain tapauksissa kaksi erillistä stimulaatiokelaa. Suurempi kelamäärä mahdollistaisi uudentyyppisiä stimulaatiosekvenssejä, jotka mahdollistaisivat monipuolisemman aivotoiminnan tutkimisen. Koska TMS-kelat ovat verrattain suurikokoisia, ei tätä tavoitetta kuitenkaan pystytä saavuttamaan yhdistämällä monta erillistä TMS-kelaa. Sen sijaan tarvittaisiin yksi monikanavainen (mTMS) laite, jossa eri kanavien kelat on yhdistetty yhdeksi suuremmaksi kokonaisuudeksi.

Tämän diplomityön tarkoitus on edistää osaltaan mTMS-laitteen suunnittelua. Tätä varten esitellään uusi mTMS-rakenne, jossa mTMS-kela koostuu suurikokoisista ohuista päällekkäisistä keloista. Tässä diplomityössä kehitetään ja testataan yksittäisten kelojen suunnittelumenetelmä tämäntyyppistä mTMS-kelaa varten. Diplomityössä esiteltävä rakenne ratkaisee kaksi nykyisissä mTMS-kelarakennesuunnitelmissa esiintyvää ongelmaa.

Avainsanat: monikanavainen transkraniaalinen magneettistimulaatio, TMS, mTMS, stimulaatiokela, kelasuunnittelu

Preface

This Thesis was written at the Department of Biomedical Engineering and Computational Science (BECS) at Aalto University School of Science in the first half of 2013.

I would like to thank my instructor Jaakko Nieminen and my supervisor Risto Ilmoniemi for the opportunity to learn research and scientific writing while writing my two special assignments and this Master's thesis between the summer 2011 and the spring 2013. I thank Jukka Sarvas for his excellent lecture about different methods for solving inverse problems, and the lecturers of CERN summer-student lecture series in 2012 for teaching things I thought I would never need.

Otaniemi, 27$^{\text{th}}$ May, 2013

Lari M. Koponen

Contents

List of Abbreviations

BEM	boundary element method
CAD	computer-aided design
DAC	digital-to-analog converter
EEG	electroencephalography
FEM	finite element method
GTO	gate turn-off thyristor
IGBT	insulated-gate bipolar transistor
IGCT	integrated gate-commutated thyristor
MEG	magnetoencephalography
MEP	motor-evoked potential
MOSFET	metal-oxide-semiconductor field-effect transistor
MRI	magnetic resonance imaging
fMRI	functional magnetic resonance imaging
NMF	non-negative matrix factorization
semi-NMF	semi-non-negative matrix factorization
PCA	principal component analysis
PLA	polylactic acid
SCR	silicon-controlled rectifier
SVD	singular value decomposition
TMS	transcranial magnetic stimulation
cTMS	controllable-pulse-width TMS
mTMS	multichannel TMS
nTMS	navigated TMS
rTMS	repetitive TMS

1 Introduction

The brain is the most complex organ in the human body; it consists of approximately 100 billion nerve cells, which are connected by 100 trillion synapses. Because of this complexity, brain functionality is for the most part unknown. However, certain aspects of this functionality can be studied with existing brain-research technologies. For example, functional neuroimaging, such as functional magnetic resonance imaging (fMRI), electroencephalography (EEG), and magnetoencephalography (MEG), can be used to study the response of the brain to a given stimulus, for example an image. This response can be used to determine which brain areas participate in processing the stimulus. However, knowing these areas does not reveal which area is responsible for producing a specific physiological response. This problem can be studied non-invasively with transcranial magnetic stimulation (TMS), which can directly manipulate the cortical activity of the brain. This manipulation enables finding causal relations between physiological responses and specific cortical areas, which can be used for both basic brain research and clinical use, such as presurgical brain mapping [1].

The basic principle of TMS is simple: a changing magnetic field (B-field) induces an electric field (E-field) in the brain. However, to produce an E-field with sufficient magnitude requires rate of change in the B-field of several kiloteslas per second, which requires complicated high-power electronics. TMS of the human brain was first reported by Barker *et al.* in 1985 [2]. The same research group also conducted the first clinical examination using TMS, where they found that the latency between motor-cortex stimulation and hand-muscle motor-evoked potential (MEP) is about 25 ms in healthy subjects and more for subjects with conditions altering motor conduction [3]. Barker *et al.* used a circular coil which produced a non-focal induced E-field. In 1988, a focal TMS coil design was introduced by Ueno *et al.* [4]. This coil design consists of two circular coils with opposite winding directions in plane and is nowadays known as the figure-of-eight coil. The figure-of-eight coil design is the standard design in current TMS devices.

A number of studies have shown that TMS is very sensitive to the exact coil position and relatively sensitive to the coil orientation. In the early 90s, Brasil-Neto *et al.* discovered experimentally that the maximal motor response for TMS is obtained when the induced E-field is approximately perpendicular to the central sulcus [5]. A few years later, Miranda *et al.* added stereotaxy, where the coil position and orientation in relation to the head are recorded in the head coordinate system, to TMS [6]. This combination of TMS and stereotaxy is known as navigated TMS (nTMS); modern nTMS systems can have less than 6 mm total error between the computed and true stimulus site in the cortex [1], which allows for reproducible stimuli required, *e.g.*, for the mentioned mapping of the brain functions.

In current systems, the TMS coil is first manually positioned and then held in place by the person operating the device. Because a typical TMS coil weights approximately 2 kg, this method has two apparent complications: an exact coil position is hard to obtain and hard to maintain for prolonged periods, and moving the coil from one position to another can take several seconds. These complications

could be avoided by using multiple stimulating coils, a linear combination of which would produce the stimulus.

The concept of a multichannel-TMS (mTMS) device was presented by Ilmoniemi and Grandori in 1993, [7]. The first mTMS coil design was published by Ruohonen and Ilmoniemi in 1996 in Ref. [8]. Their design consisted of small circular coils in a square or hexagonal lattice, which allowed adjusting the focality, location, and orientation of the stimulus without moving the coils. However, this design contains several difficulties that render building such an mTMS device impractical. For example, making the individual coils smaller reduces their coupling with the cortex (thus increasing the power consumption and the heating of the coils for a similar-intensity stimulus) whereas making them larger reduces the positional accuracy of the system, the coils couple with each other complicating controlling individual coils, and the amount of channels required for covering large areas is in the order of one hundred. Various improvements to this design have been proposed and they will be evaluated in Section 3.1. However, none of these improvements addresses all of these difficulties.

In order to overcome these problems, this Thesis proposes a novel approach for mTMS that employs large thin overlapping coils. This Thesis is organized as follows. Chapter 2 reviews the methods for computing TMS-induced E-field, introduces the inverse problem for TMS-induced E-field, calculates the scaling laws for the heating of TMS coils, and evaluates the suitability of existing TMS power electronics for use in mTMS. Chapter 3 reviews the existing mTMS designs, introduces two new methods for designing suitable overlapping TMS coils, and presents a method for designing a coil former for these coils. Chapter 4 validates the design methods by building a prototype mTMS coil and measuring its induced E-field.

2 Theory

The previous chapter summarized the history of TMS-coil development and introduced the reader with existing mTMS design. This chapter will present methods for computing the TMS-induced E-field and the heating of the coil caused by a stimulation. Also, Section 2.4 assesses suitability of various TMS-stimulator power electronics for mTMS.

2.1 TMS-induced E-field

The TMS-induced E-field is governed by the four Maxwell's equations:

$$\nabla \cdot \boldsymbol{E} = \frac{\rho}{\varepsilon_0} \,, \tag{1}$$

$$\nabla \cdot \boldsymbol{B} = 0 \,, \tag{2}$$

$$\nabla \times \boldsymbol{E} = -\frac{\partial \boldsymbol{B}}{\partial t} \text{ , and} \tag{3}$$

$$\nabla \times \boldsymbol{B} = \mu_0 \boldsymbol{J} + \mu_0 \varepsilon_0 \frac{\partial \boldsymbol{E}}{\partial t} \,; \tag{4}$$

where $\boldsymbol{E}$ is the E-field, $\boldsymbol{B}$ is the B-field, $\boldsymbol{J}$ is the current density, ρ is the charge density, ε_0 is the vacuum permittivity, and μ_0 is the vacuum permeability. A medium has polarization $\boldsymbol{P}$ and magnetization $\boldsymbol{M}$ which can be used to define auxiliary fields

$$\boldsymbol{D} = \varepsilon_0 \boldsymbol{E} + \boldsymbol{P} \tag{5}$$

and

$$\boldsymbol{H} = \frac{1}{\mu_0} \boldsymbol{B} + \boldsymbol{M} \,. \tag{6}$$

Defining bound charge density $\rho_\mathrm{b} \equiv -\nabla \cdot \boldsymbol{P}$, free charge density $\rho_\mathrm{f} \equiv \rho - \rho_\mathrm{b}$, bound current density $\boldsymbol{J}_\mathrm{b} \equiv \nabla \times \boldsymbol{M} + \partial \boldsymbol{P}/\partial t$, and free current density $\boldsymbol{J}_\mathrm{f} \equiv \boldsymbol{J} - \boldsymbol{J}_\mathrm{b}$, we can rewrite Eq. 1 as

$$\nabla \cdot \boldsymbol{D} = \rho_\mathrm{f} \tag{7}$$

and Eq. 4 as

$$\nabla \times \boldsymbol{H} = \boldsymbol{J}_\mathrm{f} + \frac{\partial \boldsymbol{D}}{\partial t} \,. \tag{8}$$

2.1.1 Time-harmonic solution

A TMS pulse can be modeled as a sinusoidal oscillation with the angular frequency $\omega = 2\pi f$, if the the transient effects at the beginning and at the end of the pulse are neglected. This allows using time-harmonic Maxwell's equations, where the fields are expressed in the frequency domain instead of the usual time domain.

In case of linear and isotropic medium, the auxiliary fields and the free current density are expressed as

$$\boldsymbol{D} = \varepsilon \boldsymbol{E} \ , \tag{9}$$

$$\boldsymbol{H} = \frac{1}{\mu}\boldsymbol{B} \ , \text{ and} \tag{10}$$

$$\boldsymbol{J}_\mathrm{f} = \sigma \boldsymbol{E} \ ; \tag{11}$$

where ε is the permittivity, μ is the permeability, and σ is the conductivity of the medium. A partial differential equation for $\boldsymbol{H}$ can be obtained by solving $\boldsymbol{E}$ from Eq. 8 using Eqs. 9–11 and substituting it to Eq. 3:

$$\nabla \times \left[\frac{\nabla \times \boldsymbol{H}}{\sigma + i\omega\varepsilon} \right] = i\omega\mu\boldsymbol{H} \ , \tag{12}$$

where $i = \sqrt{-1}$. This equation can then be solved using the finite element method (FEM) [9]; when the H-field is known, the E-field can be computed using the fourth Maxwell's equation and Ohm's law (Eq. 4 and Eq. 11, respectively).

When FEM is used, ε, μ, and σ can vary as functions of position. Thus, this method allows modeling variable conductivity of the medium and variable magnetic permeability, like a magnetic core in the coil. This method was used by Deng *et al.* in Ref. [10], where they computed TMS-induced E-fields for 50 different TMS-coil designs. However, this formulation is not the only time-harmonic formulation. The E-field can also be solved from the time-harmonic version of the third Maxwell's equation using independent-impedance method [11], which allows modeling also the anisotropy in tissue [12].

The biggest issue with all time-harmonic methods is their slow performance; for example, it took four hours of computation time to reach a 2-% relative error in TMS-induced E-field with 2-mm spatial resolution using the independent-impedance method [12].

2.1.2 Quasi-static solution

The rise-time of a TMS pulse is typically from 50 to 100 µs, and this is the shortest component of a TMS pulse. This rise-time equals a characteristic frequency between 2.5 and 5 kHz. With this low frequencies, the quasi-static approximation can be used for the TMS-induced E-field computation [13, 14]. The quasi-static approximation allows using the Biot–Savart law,

$$\boldsymbol{B}(\boldsymbol{r}) = \frac{\mu_0 I}{4\pi} \oint_\mathrm{coil} \frac{\mathrm{d}\boldsymbol{l}' \times (\boldsymbol{r} - \boldsymbol{r}')}{|\boldsymbol{r} - \boldsymbol{r}'|^3} \ , \tag{13}$$

where I is the current in the coil and $\boldsymbol{r}$ is the position. However, this law gives the correct magnetic field only in case of infinite homogeneous medium. If the medium is assumed to consist of piecewise homogeneous regions, the magnetic field of the volume currents can be computed from the surface potentials of these regions using Geselowitz' formula [15]. These surface potentials can be solved for example with

the boundary element method (BEM), as explained in Ref. [16]. However, this method can not be applied for problems that include magnetizable medium, such as a magnetic core in the coil.

Combining these two components of the magnetic field, the TMS-induced E-field can be computed using reciprocity. First, a current dipole is placed inside the head, then its magnetic field through the TMS coil is computed (this includes calculating the magnetic field of the dipole using the Biot–Savart law and the magnetic field of the volume currents using Geselowitz' formula). If the current dipole oscillates, the magnetic flux through the TMS coil varies, inducing an electromotive force in the coil; because of reciprocity, an oscillating current in the coil will induce the same electromotive force in the current dipole. This kind of method was used, for example, by Im and Lee in Ref. [17]. If the human head is assumed to consist of only few homogeneous isotropic conductivity regions with relatively simple surface geometry, the quasi-static solution is significantly faster to compute than the time-harmonic solution. However, the computation can still last several hundred seconds.

2.1.3 Quasi-static solution in spherically symmetric geometry

The TMS-induced E-field computation problem is simplified further in an isotropic, spherically symmetric conductor. Now, the volume currents from the previous section (Section 2.1.2) can be replaced with suitable line currents whilst the external magnetic field remains unchanged [18]. In MEG, this is called *the triangle phantom* [19]. Thus, there is no need for computing the surface potentials and the TMS-induced E-field can be solved by calculating the mutual inductance between the triangle phantom and the coil.

This mutual inductance can be calculated by discretizing the coil into short line segments and then using the inductance formulas from Ref. [20]. For coils presented as continuous surface currents, a different approach for computing the mutual inductance using the fourth Maxwell's equation, Ampère's circuit law with Maxwell's correction, is shown in Ref. [21]. In this method, the current density in the region of interest and the Maxwell's correction term are assumed to be neglible. Thus,

$$\nabla \times \boldsymbol{B} = 0 \ , \tag{14}$$

and the magnetic field can be represented with the magnetic scalar potential. Using the boundary condition for the magnetic field,

$$\boldsymbol{B}_{\text{ext}} - \boldsymbol{B}_{\text{int}} = \mu_0 \cdot \boldsymbol{K} \times \boldsymbol{n} \ , \tag{15}$$

where $\boldsymbol{B}_{\text{ext}}$ is the B-field outside and $\boldsymbol{B}_{\text{int}}$ is the B-field inside the surface current boundary, $\boldsymbol{K}$ is the surface current density and $\boldsymbol{n}$ is the surface normal vector, one can solve the magnetic field, and thus the magnetic flux through an infinitesimal triangle phantom. With this method, one can obtain analytical expression for the TMS-induced E-field for multiple coil geometries, such as concentric spherical current shells [21], non-concentric spherical current shells, and planar current surfaces. In the simplest geometry, the concentric spherical current shells, the TMS-induced E-field

for a surface current,

$$\boldsymbol{K}(r = R, \theta, \phi, t) = f(t)\frac{\hat{\boldsymbol{Y}}^m_{l,l}(\theta, \phi)}{R} \ , \tag{16}$$

where R is the radius of the surface current distribution, $\hat{\boldsymbol{Y}}^m_{l,l}$ is a real vector spherical harmonic, and $f(t)$ is the time-dependency (in amperes), is

$$\boldsymbol{E}(r < R, \theta, \phi, t) = -\mu_0 \frac{\partial f(t)}{\partial t} \frac{1}{2l+1} \left(\frac{r}{R}\right)^l \hat{\boldsymbol{Y}}^m_{l,l}(\theta, \phi) \ . \tag{17}$$

The magnetic field of this surface current stores energy

$$U = \frac{\mu_0}{2} \frac{f(t)^2 R}{2l+1} \ . \tag{18}$$

Because the real vector spherical harmonics form a complete orthogonal set of surface current densities, all spherical current densities can be expressed as a linear combination of these current densities. This analytical, series solution provides rapid TMS-induced E-field computation allowing for example TMS-coil optimization [21, 22].

2.2 TMS-induced E-field inverse problem

The previous section introduced methods for computing the TMS-induced E-field. These methods are useful for computing the effect of TMS; but, for designing a TMS coil, their inverse—which coil produces the given induced E-field—would be much more useful. This section introduces this TMS-induced E-field inverse problem.

As Heller and van Hulsteyn showed in 1992, the induced E-field maximum is always at the surface of a uniform conductance region [23]. For spherically symmetric geometry, which the head resembles to some extend, the induced E-field maximum is always at the surface regardless of the conductance distribution. These mean that it is not possible to have depth-focality in TMS. Thus, the TMS-induced E-field inverse problem is very ill-posed, as most E-field patterns are impossible to induce with TMS. However, if the E-field is determined only on one surface, the problem becomes less ill-posed.

Intuitively, higher spatial frequencies are harder to induce than lower ones. This is because the field has smaller characteristic dimensions, and thus the B-field will decay faster with increasing distance from the coil. This suggests that the induced E-field will be weaker at the cortex, which can actually be shown for spherically symmetric geometry where the weakening near the surface is approximately exponentially proportional to the inverse surface area of that feature (A_{feature}) [21]. This relation can be seen from Eq. 17. According to this equation, the induced E-field is proportional to $(r/R)^l$, where r/R is the ratio between target and coil radii, and $l \precsim 1/A_{\text{feature}}$ is the degree of the spherical harmonic component, which tells us the number of nodal lines for that spherical harmonic component. Thus, for fixed radii, the induced E-field is approximately exponentially proportional to the inverse surface area of that feature.

Because TMS is reciprocal to MEG, the TMS inverse problem resembles the well-known EEG/MEG inverse problem. This resemblance was used by Ruohonen and Ilmoniemi for transforming computing the needed rate of change in coil currents in an mTMS device into linear algebra in Ref. [8]. Here, their approach is generalized by replacing the coils with continuous surface currents. The problem is to reproduce a continuous E-field distribution with time-varying continuous surface currents. This problem can be discretized into a discrete problem with m time varying current components (a linear combination of which forms the coil) which induce n E-field components:

$$\boldsymbol{p} = \mathbf{M}\boldsymbol{i} \ , \tag{19}$$

where $\boldsymbol{p}$ is an n-component vector describing the induced E-field, $\mathbf{M}$ is an $m \times n$ lead-field matrix, and $\boldsymbol{i}$ is an m-component vector describing the rate of change in the m current components. When the problem is discretized, the number of points, m and n, can be chosen arbitrarily. However, in MEG, there are far less degrees of freedom for the coils than for the brain activity. A recent estimate suggested that there are less than 100 degrees of freedom in MEG data [24]. The number of degrees of freedom for a TMS coil is of the same order of magnitude [21]. The number of degrees of freedom for induced E-field in the brain is significantly higher than this. Thus, for TMS, it is reasonable to select $m \ll n$. With this choice, the TMS inverse problem is overdetermined whereas the EEG/MEG inverse problem is underdetermined. This will likely cause new problems with the known inverse-problem solving methods.

2.2.1 Evaluating different methods for solving the inverse problem

The orthogonal series presentation of the TMS-induced E-field in spherically symmetric geometry resembles Fourier series without the constant term. Thus, the Fourier series can be used to estimate the performance of different methods in solving the inverse problem. Let us assume that the cost (*i.e.*, the magnetic field energy) is linearly proportional to the square of the spatial frequency.

The TMS inverse problem is overdetermined; that is, there are more constraints than there are degrees of freedom. Thus, there is no exact solution for it. The simplest optimization formulation for the overdetermined problem is to minimize the norm between the desired E-field, $\boldsymbol{e}$, and the TMS-induced E-field, $\boldsymbol{p} = \mathbf{M}\boldsymbol{i}$. This approach was used by Ruohonen and Ilmoniemi in Ref. [8], and it is known as the least-squares estimation,

$$\min ||\mathbf{M}\boldsymbol{i} - \boldsymbol{e}||^2 \ , \tag{20}$$

where $\mathbf{M}$ is the lead-field matrix, $\boldsymbol{i}$ is the distribution of coil currents, and $\boldsymbol{e}$ is the distribution of induced electric field. A least-squares solution for focal TMS-stimulus is shown in Fig. 1. The solution is obtained using formula

$$\boldsymbol{i} = \left(\mathbf{M}^\top \mathbf{M}\right)^{-1} \mathbf{M}^\top \boldsymbol{e} \ . \tag{21}$$

Unlike the minimum norm solution for an underdetermined inverse problem, which produces a wide distribution with minimum signal power, this solution suffers from the Gibbs phenomenon (oscillations in the induced E-field) and high energy cost.

The simplest way to mitigate the high energy cost is to reduce the number of components, that is, to truncate the series. However, truncating the series does not yield a »smooth»[1] induced E-field. This can be fixed by using Tikhonov regularization [25], which transforms Eq. 20 into

$$\min ||\mathbf{M}\boldsymbol{i} - \boldsymbol{e}||^2 + ||\mathbf{\Gamma}\boldsymbol{i}||^2 \ , \tag{22}$$

where $\mathbf{\Gamma}$ is the Tikhonov matrix, which is (here) a diagonal matrix of the individual component costs multiplied by a positive constant λ. The resulting field is shown in Fig. 2 for two values of regularization constant. The solution is obtained using formula

$$\boldsymbol{i} = \left(\mathbf{M}^\top\mathbf{M} + \mathbf{\Gamma}\right)^{-1}\mathbf{M}^\top\boldsymbol{e} \ . \tag{23}$$

The Tikhonov regularization works well for the problem; however, it weights the error in the zero-field regions as much as the error in the high-field regions. This is not ideal behavior, as both Hodgkin–Huxley model for individual neuronal cells [26] and TMS experiments suggest a threshold for neuronal response. Thus, the error in the zero-field regions should be less significant than the error in the high-field regions. This differing importance can be partially accounted using weighted least-squares; however, an alternative approach is to move from inverse problem into a general constrained optimization problem. In this optimization problem, the field is required to have certain characteristics (Fig. 3, the field magnitude can not be in the light blue regions) and the minimum-cost solution fulfilling these constraints is searched. This approach was used to optimize a TMS-coil in Ref. [21], where it was shown to be a convex optimization problem with convex feasibility set. Selecting the constraints is addressed in greater detail in Ref. [22].

2.3 Heating of TMS coils

The inductance of a typical TMS coil is $L = 10\,\mu\mathrm{H}$, and a maximum-strength TMS pulse has approximately $I_{\mathrm{peak}} = 10\,\mathrm{kA}$ peak current [27]. Thus, the maximum energy stored in a TMS coil is approximately

$$U = \frac{1}{2}L\left(I_{\mathrm{peak}}\right)^2 = \frac{1}{2}\cdot 10\,\mu\mathrm{H}\cdot(10\,\mathrm{kA})^2 = 500\,\mathrm{J} \ . \tag{24}$$

This energy is similar to that of a 9-mm pistol round[2]. As the TMS-pulse rise-time is 50–100 µs, the average power during the pulse is 5–10 MW. This Thesis, however, considers a weaker stimulus with 5-kA peak current and 50-µs rise-time, halving the power and reducing the stored energy to one fourth. None of this energy is recovered in a monophasic TMS stimulus; in case of a biphasic TMS stimulus only 25–65% of the energy is recovered [27, page 15]. The non-recovered energy is dissipated as heat somewhere in the TMS device[3].

[1] The field is smooth in mathematical sense; however, it is oscillatory in the spatial domain.

[2] Typical muzzle energy for 9×19-mm Parabellum: $U = \frac{1}{2}mv^2 = \frac{1}{2}\cdot 8\,\mathrm{g}\cdot(340\,\mathrm{m/s})^2 = 460\,\mathrm{J}$.

[3] A negligible amount of the energy is dissipated to heat the head and to produce the coil click.

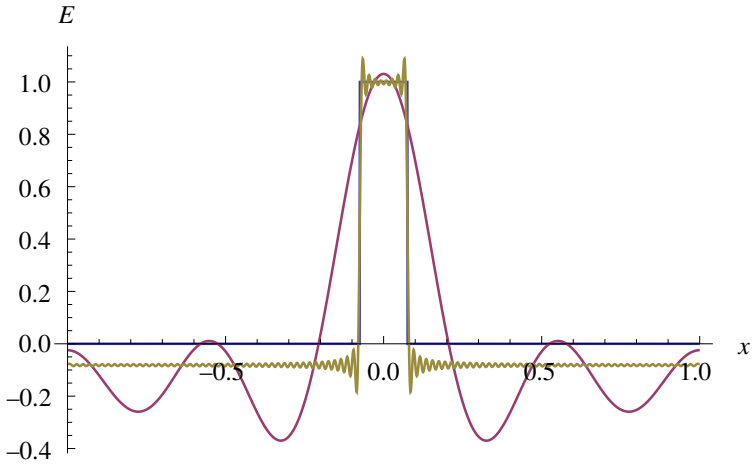

Figure 1: A least-squares solution for the inverse problem. **Blue:** the target E-field. Truncated series: **yellow**, 100 terms; or **red**, 4 terms; the costs are 24 arb. units and 1.8 arb. units, respectively.

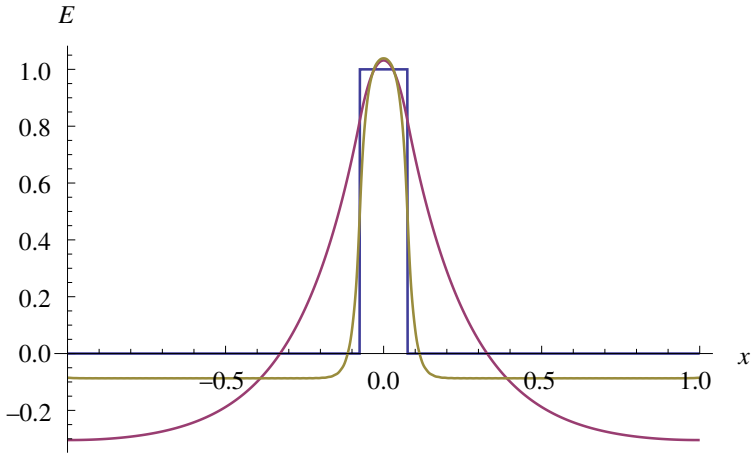

Figure 2: A Tikhonov-regularized least-squares solution for the inverse problem. **Blue:** the target E-field. Two different values for the regularization constant: **yellow**, small constant, cost 3.3 arb. units; and **red**, large constant, cost 0.8 arb. units.

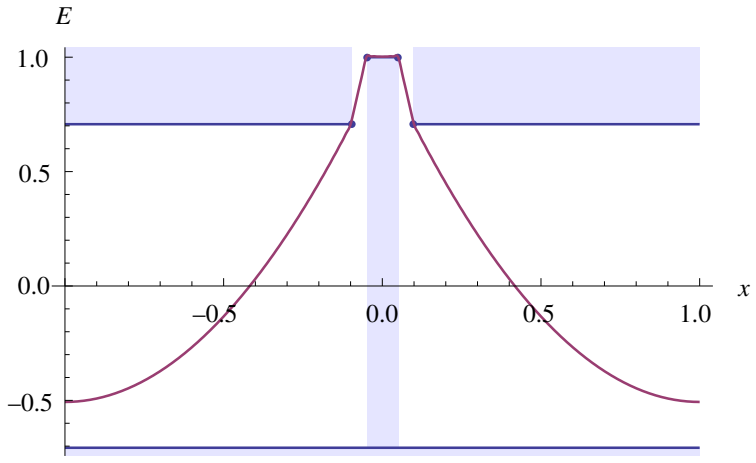

Figure 3: A solution by constrained optimization, cost 0.8 arb. units.

Let us examine resistive heating of a piece of a coil wire with length l, cross-sectional area A, density ρ, conductivity σ, and specific heat capacity c. There are two frequency-dependent electromagnetic effects affecting the coil heating at high frequencies: the skin effect and the proximity effect. The skin effect causes most of the current to flow near the surface at high frequencies, reducing the effective wire cross-section; however, this effect can be mitigated at typical TMS stimulus frequencies by using Litz wire. The proximity effect is caused by the interaction between nearby wires, and similarly to the skin effect it reduces the effective wire cross-section. The remainder of this section ignores these effects, but the former will be revisited in Section 4.1.

The piece has resistance

$$R = \frac{l}{\sigma A} \ , \tag{25}$$

and mass

$$m = \rho l A \ . \tag{26}$$

Thus, its heat capacity is

$$C = cm = c\rho l A \ . \tag{27}$$

According to Joule heating and Ohm's law, the power dissipated in a resistor is

$$P(t) = R[I(t)]^2 \ , \tag{28}$$

where $I(t)$ is the current flowing through the resistor. Assuming a TMS pulse has sinusoidal shape, $I(t) = I_{\text{peak}} \sin(\pi t/\Delta t)$, from $t = 0$ to Δt we obtain that the energy dissipated in the coil is

$$U = \frac{R\left(I_{\text{peak}}\right)^2 \Delta t}{2} \ , \tag{29}$$

and the temperature change is

$$\Delta T = \frac{U}{C} = \frac{\left(I_{\text{peak}}\right)^2 \Delta t}{2c\sigma\rho A^2} \ . \tag{30}$$

Substituting the heat capacity, the conductivity, and the density of copper (Table 1) into Eq. 30, it is obtained for a 5-kA peak current with a 100-µs stimulus duration in a circular copper filament with diameter d:

$$\Delta T = \frac{8\left(I_{\text{peak}}\right)^2 t_{\text{duration}}}{c\sigma\rho\pi^2 d^4} \approx \frac{10\,\text{K}}{\left(d/1\,\text{mm}\right)^4} \ ; \tag{31}$$

or, alternatively,

$$\Delta T \approx \frac{6\,\text{K}}{\left(A/1\,\text{mm}^2\right)^2} \ . \tag{32}$$

Table 1: Properties of copper.

Quantity (symbol)	Value
density (ρ)	$8960\,\mathrm{kg\,m^{-3}}$
conductivity (σ)	$59.6\,\mathrm{MS\,m^{-1}}$
heat capacity (c)	$385\,\mathrm{J\,kg^{-1}\,K^{-1}}$

2.4 TMS-stimulator power electronics

The conventional monophasic TMS-stimulator circuit diagram is depicted in Fig. 4. A TMS stimulator needs a fast high-power high-voltage switch. The high voltage prevents using metal-oxide-semiconductor field-effect transistors (MOSFETs), and the fast triggering requirement prevents using electromagnetic relays. The easiest approach is to use a thyristor such as a silicon-controlled rectifier (SCR). The SCR is opened by a rapid voltage rise in its gate by the trigger circuit. However, once the SCR is opened, it can not be closed before the coil current is close to zero.

The stimulator consists of a storage capacitor C, which is typically a polarized electrolytic capacitor with approximately 200-µF capacitance and 3-kV maximum voltage; a high-power diode protecting the capacitor and the power supply from reverse polarity; an SCR used as a switch; and the stimulating coil, with approximately $L = 10\,\mu\mathrm{H}$ inductance. These four components have total resistance of approximately $R = 50\,\mathrm{m\Omega}$. This circuit was modeled using Simulink (MATLAB R2012b); initially the circuit behaves like an LC-oscillator and later like an RL-damping (Fig. 6). Thus, the stimulus rise-time for a traditional monophasic TMS stimulator can be estimated to be

$$t_{\text{rise-time}} \approx \frac{2\pi\sqrt{LC}}{4}\ . \tag{33}$$

In 2008, Peterchev *et al.* presented a more-controllable version of the monophasic TMS stimulator [28], a schematic presentation of which is shown in Fig. 5. The basic idea is to replace the SCR with an insulated-gate bipolar transistor (IGBT). This IGBT allows disconnecting the capacitor from the coil at any time, which allows controlling the pulse width. Now, the capacitor can have much higher capacitance, making it a near-constant voltage source, which makes the TMS pulse more rectangular. However, when the TMS coil with non-zero current is disconnected from the capacitor, a voltage spike is induced. This spike can be dissipated by a snubber circuit (a freewheeling diode and a few small-capacity capacitors and low-resistance resistors in parallel with the IGBT to protect it from the spike, and a small capacitor in parallel with the storage capacitor to protect it from the spike), which is shown in their article. This circuit was also modelled using Simulink (Fig. 6).

The IGBT circuit has the advantage of reduced power consumption and heating of the coil. Peterchev *et al.* [28] report that these are reduced by 25% and 70%, respectively, compared to the sinusoidal pulse producing similar neuronal depolarization. This reduction is achieved by having a shorter current rise-time and more-constant derivative of current during the current rise, which allow a reduced peak current.

Recently there has been some research in advanced cTMS, where the TMS pulse waveform can be controlled more freely. In 2011, Peterchev *et al.* presented a half-bridge cTMS device capable of both mono- and biphasic TMS [29]. Unlike the conventional TMS power electronics, this design is symmetric. That is, it can produce a first-negative-current stimulus. Later, Peterchev *et al.*, compared their half-bridge device to a full-bridge device [30]. The former requires two IGBTs whereas the latter requires four IGBTs. However, the latter does not require active snubber circuit in parallel with the coil, and it allows IGBTs with lower voltage rating. The latter also allows for more flexible pulse shaping. Because of these advantages, they recommended using the latter design, whose circuit diagram is shown in Fig. 7.

In 2012, Goetz *et al.* proposed a different approach to the high-voltage problem. Their proposed design is a series connection of N low-voltage H-bridges, which makes the design essentially a high-power parallel digital-to-analog converter (DAC) with $2N + 1$ quantization levels (Fig. 8) [31]. As the maximum voltage over each switch in each module is at most the voltage in that modules capacitor, this design can employ ordinary high-power MOSFETs instead of more expensive high-power, high-voltage semiconductors, such as IGBTs, GTOs (gate turn-off thyristors), and IGCTs (integrated gate-commutated thyristors). The design allows arbitrary waveforms, including for example a conventional-looking monophasic pulse with energy recovery. However, it is unclear whether this kind of TMS stimulator could be built with a reasonable price tag and size.

2.4.1 mTMS-stimulator power electronics

This subsection assesses whether the previously mentioned TMS control electronics are suitable for an mTMS device. Four mTMS-specific problems are evaluated, concerning the simultaneous operation of the different coils.

Simultaneity. An mTMS device requires that all channels can be triggered simultaneously. Because a TMS-pulse rise-time is from 50–100 µs, this simultaneity needs to be at least within a few microseconds. This level of simultaneity can be achieved with both the conventinal TMS design and the mentioned cTMS designs, as SCRs and IGBTs are turned on by gate voltage (which can be common for all channels) and have a turn-on time and delay of a few microseconds [32, 33]. Thus, both designs can be made simultaneous enough.

Stimulation phase matching. However, in conventional TMS design, phase matching is needed. That is, $\omega = 1/\sqrt{LC}$ must be same for all channels. The high-power high-voltage capacitors used in TMS do not have adjustable capacitance; thus, the coil inductance must be tunable. Although this can be achieved with (small-inductance) tunable inductor in series with each coil, the device would be susceptible to capacitor non-linearity and temperature dependency. With the cTMS design there is no need for phase matching.

Stimulation polarity. The mentioned conventional monophasic TMS stimulator, the mentioned monophasic cTMS stimulator, and the conventional biphasic TMS stimulator [27, page 15] all share similar asymmetry that the initial capacitor charge must be positive. However, this is not a severe problem as it can be fixed

either by adding an H-bridge around each coil (Fig. 9) or by suitable coil design (Section 3.2.2). In contrast to the conventional TMS-stimulator power electronics, the advanced cTMS-stimulator power electronics can generate both positive and negative initial voltages. Thus, they might suit mTMS better than the conventional power electronics.

Coil coupling. In general, there will be mutual inductance between the different coils in an mTMS device. In an mTMS device, the coupling coefficient, k_{ij},

$$M_{ij} = k_{ij}\sqrt{L_i L_j} \ , \tag{34}$$

can have a magnitude close to unity. This will cause two problems. First, the coupling can induce large voltages into other coils. However, if the coil inductances are similar to each other the induced voltage can not be larger than the largest capacitor voltage:

$$|V_{\text{induced, 2}}| = |M_{12}\dot{I}_1| = |k|\sqrt{L_1 L_2}|\dot{I}_1| \leq \sqrt{L_1 L_2}|\dot{I}_1| \approx L_1|\dot{I}_1| = |V_{\text{capacitor, 1}}| \ . \tag{35}$$

Second, the mutual inductance couples the changing speeds of the coil currents. As previously noted by Han *et al.* this coupling can be compensated by correct selection of initial voltages [34]. The voltages can be obtained from

$$\boldsymbol{V} = \mathbf{L}\frac{\partial \boldsymbol{I}}{\partial t} \ , \tag{36}$$

where $\boldsymbol{V}$ is the vector of the initial voltages, $\mathbf{L}$ is the (mutual) inductance matrix of the system, and $\partial \boldsymbol{I}/\partial t$ is a vector of the desired changing speeds in the coil currents. However, as noted in the previous paragraph, conventional TMS power electronics do not support negative initial voltages. Thus, to solve this problem, the H-bridges from previous paragraph may be needed even for all-positive coil currents, or the mutual inductances must be made non-negative.

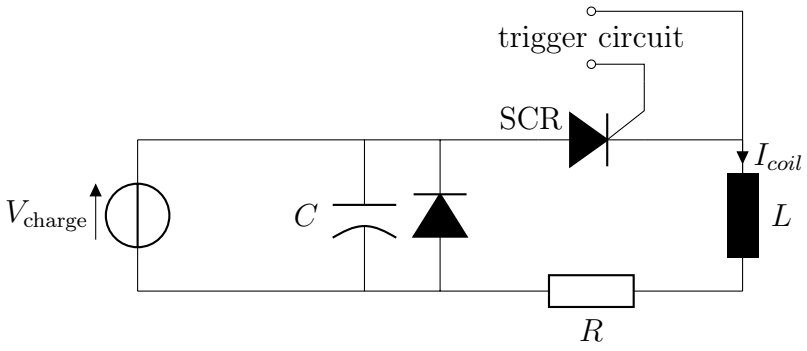

Figure 4: The circuit diagram for monophasic TMS stimulator [27, page 14].

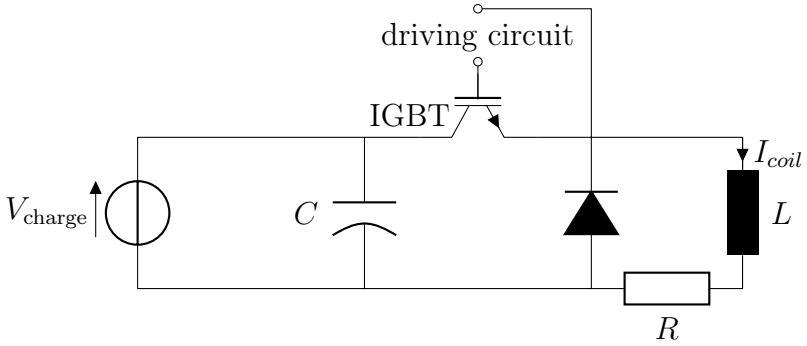

Figure 5: A simplified circuit diagram for a monophasic cTMS stimulator [28].

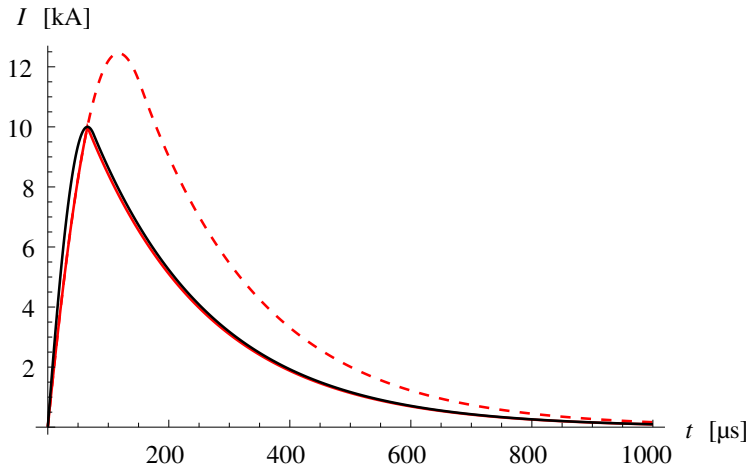

Figure 6: The current in monophasic TMS coil. **Black:** Using SCR; the capacitance was 200 µH, and the initial capacitor voltage was 2635 V. **Red, solid:** Using IGBT; the capacitance was 711 µH, and the initial capacitor voltage was 1990 V. **Red, dashed:** The IGBT circuit in case the IGBT could not be turned off; the extra energy from the capacitor will induce a considerably stronger stimulus, which could be potentially dangerous in some case.

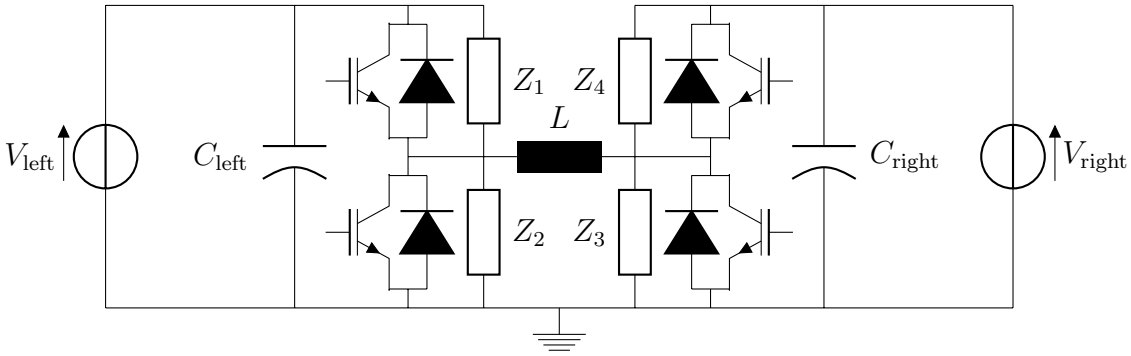

Figure 7: A full-bridge "all-phasic" cTMS-stimulator circuit diagram by Peterchev *et al.* [30]. Z_1, Z_2, Z_3, and Z_4 are capacitive snubbers protecting the IGBTs, and their structure is described in Ref. [29]. As a stimulus pattern can move energy from one capacitor to the other, there should be a two-way power supply between the capacitors in addition to the two shown power supplies.

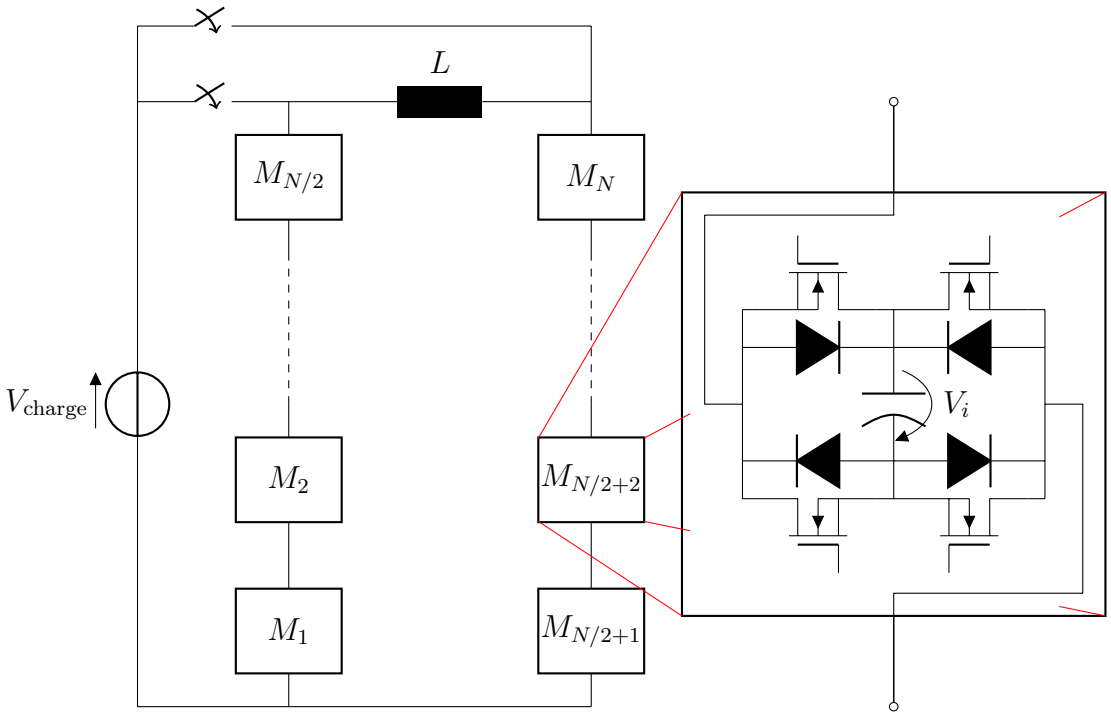

Figure 8: A series "all-phasic" cTMS-stimulator circuit diagram by Goetz *et al.* [31]. The circuit consists of N identical (low-voltage) H-bridge modules M_i, $i = 1, \ldots, N$.

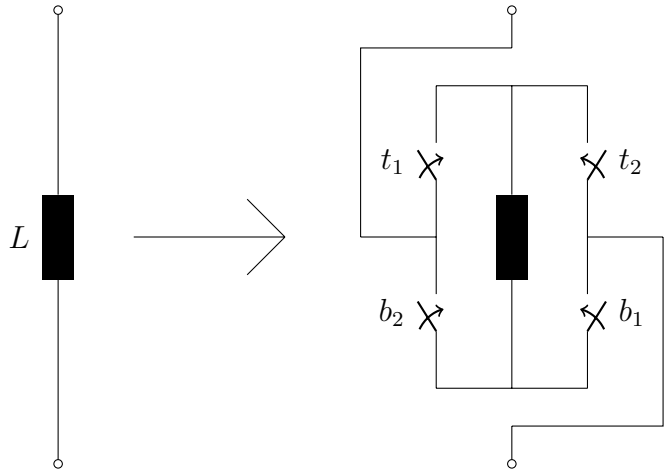

Figure 9: A H-bridge that allows electronically swapping the coil polarity. When t_1 and b_1 are closed the coil has normal polarity, and when t_2 and b_2 are closed it has inverse polarity. The switches can be implemented with slow electromagnetic relays because they are not operated during a TMS-pulse.

3 Methods

The previous chapter presented TMS-induced E-field computations and its inverse problem. This chapter will first summarize earlier methods used for mTMS development, and after that, this chapter will introduce two approaches for generating suitable overlapping TMS coils. After that, Section 3.3 discusses a method for building the coil former for an mTMS device with overlapping coils.

3.1 Previous mTMS designs

The first mTMS design was made by Ueno *et al.* in 1988 [4]. This article is also known as the first occurrence of a figure-of-eight coil design, but the article presents a method for focal TMS by having two circular coils with opposite time varying currents. Then, this principle was demonstrated by constructing the first figure-of-eight coil (*i.e.*, a coil where the two circular coils have been fixed to each other).

Ruohonen and Ilmoniemi presented the first truly multichannel mTMS design using small circular coils in a square lattice (Fig. 10 A) in 1996 [8]. In that paper, they presented least-squares solution for solving the required rate of change in the coil currents. As shown in Section 2.2.1, this method suffers from Gibbs phenomenon: it gives high-energy, high-accuracy solutions with large oscillations at the maximum spatial frequency of the lattice.

Later, the same authors also presented an mTMS design using small circular coils in a hexagonal lattice (Fig. 10 B) [35]. However, this article was about the effects of coil size on system focality, which was defined as the area with field above half of the maximum value. The focality was optimized using Rosenbock optimization method [36], which is an adaptive coordinate-descent method. The optimization problem in Ref. [35] is to minimize the focal area at any energy cost as opposed to optimization method in Ref. [21], where a minimum-energy solution is searched for given focality.

The square lattice mTMS coil was analyzed in Ref. [37], where its ability to focus the stimulation into a given stimulation site was computed. This article considered using the coils for stimulating peripheral-axon stimulation, not TMS. Thus, the article used cylindrical geometry and determined the stimulus site based on maximum induced E-field gradient (instead of maximum induced E-field magnitude). However, most of their analysis result apply to TMS. When the coils were positioned 20 mm above the target region, the maximum position error was found to be in the order of half the coil diameter, for coils with 30-mm diameter. This essentially means that the induced E-field maximum is always located between two adjacent coils. For 20-mm diameter coils, this maximum position error was only 3 mm, which means that the stimulation site can be positioned arbitrarily. This result means that such a small-coil mTMS device requires at least hundred channels for whole-head coverage.

Since then, this small-coil mTMS design has been studied in several research articles, and several improvements for it have been suggested. For example, Han *et al.* considered the effects of coil coupling and proposed an improvement to the spatial localization of the square-lattice design [34]. The idea is to make two layers of partially overlapping square lattices, one of which has a half-coil-diameter offset

(Fig. 10 C). However, this design fails to acknowledge that small circular TMS coils are relatively thick, moving the upper layer too far from the head for effective stimulus.

Im and Lee [17] analyzed the induced E-field by a quasi-regular lattice of non-overlapping small coils in realistic head geometry. In their design, each lattice position had either one, two, or three orthogonal orientation small circular coils or two parallel coils placed on top of each other (similarly to an MEG radial gradiometer). This article found that the last design offers the best compromise between number of channels and mean position error (10 mm with 102 coil units (two coils each), which was the same as for three orthogonal small coils per position, and better than 14-mm error obtained with only one coil at each location). However, the field computations in the article considered only the E-field component normal to the cortex, and the article did not analyze the energy required for stimulation. Similarly to Ref. [34], the article did not consider how the coils would physically be fit inside each other.

Jiang *et al.* [38] presented a new design proposal for mTMS, the wire-mesh coil which consists a mesh of anterior–posterior and mediolateral straight conductors (Fig. 10 D). This design can reduce the channel count of mTMS device significantly. However, the system, as described in the article, has a discrete spatial resolution (that of the wire spacing) and discrete induced E-field orientations (90° increments). As shown in the article, this design suffers also from reduced focality as the cortex is stimulated everywhere along the wire, not only at the desired target region.

The mTMS research seems to be focused around using multiple similar-shaped small coils. This approach has an apparent benefit: each coil unit has the same inductance; thus, each coil unit can use similar power electronics for similar stimulation time evolution. Also, optimizing an mTMS device consisting of self-similar units is much simpler because of less degrees of freedom. This kind of coil optimization has been done in a few articles including Refs. [39, 40, 41].

However, despite these optimizations, all small-coil mTMS designs share a common weakness. The small coils, due to their size, require considerably higher rise speed of current, and thus higher maximum current. This causes problems with the stimulator power consumption and the heating of the coils. To illustrate this problem, the TMS-induced E-field of a small-circular coil mTMS and wire-mesh mTMS designs were computed. The computed induced E-fields are shown in Fig. 11. Delivering a 100-V/m stimulus with 50-µs rise-time to one site at the cortex requires mean stimulation power of 6.5 MW and 18 MW for 30-mm and 20-mm coils, respectively, whereas the wire-mesh design requires 42-MW mean stimulation power for a focal stimulus. In case of the small circular coils, the 1-turn coils would require a peak current of 66 kA and 140 kA, respectively. The current can be reduced by using multiple turns. However, this would not affect the power requirements as dropping the current n-fold increases the voltage n^2-fold. Surprisingly, the power requirements for 20-mm coils can be lowered significantly by using the constrained optimization formulation from Section 2.2 for solving the individual coil currents. The mean stimulation power was reduced to 5.0 MW and the maximum 1-turn currents to 50 kA for a 70-mm-figure-of-eight-focality-like stimulus. The wire-mesh coil requires a maximum current of 74 kA. Ref. [38] suggests using only one wire per line, and although there

exists power electronics (almost) capable of that[4] they are too expensive for TMS use.

In addition to the mentioned small-coil designs, there are some mTMS designs using existing TMS equipment. One of these is to use two coils that revolve around the head, Ref. [43]. However, with this approach the stimulus of two different sites can never be simultaneous. Another solution is to use several large TMS coils for stimulus of the deeper brain structures, such as the devices depicted in Refs. [44, 45]. However, this kind of approach results in a non-focal stimulus of the cortex.

3.2 mTMS with overlapping coils

The previous section showed the limitations with existing mTMS designs. To overcome these limitations, this section presents a novel design, using large thin overlapping coils. Finding suitable coils is a two-part problem. First, to find desirable induced E-field patterns, a linear combination of which can cause the required stimuli. Second, to find the coils that produce those E-fields. There are two distinct approaches for this problem. First, a bottom-up-like approach: select a set of induced E-field patterns that can stimulate as many different positions and orientations as possible. Second, a top-down like approach: select a set of positions and orientations, compute desirable induced E-field patterns for these, and see which combinations of these patterns to use. The former approach benefits from guaranteeing optimality of the solution whereas the latter is significantly easier to compute.

In the following two sections, word 'coil' means an induced E-field pattern, which can be produced by a time-varying continuous surface current distribution that can be approximated with a coil, and is expressed with vector-valued spherical harmonics.

3.2.1 Bottom-up approach—global optimization of coverage

The bottom-up approach for overlapping mTMS coil design sounds very simple: find a set of coils that can stimulate as many different positions and orientations as possible. This is because it is already expressed as an optimization problem with simple utility function. The utility function is just the number of positions and orientations that can be stimulated with the given coils, and testing whether a given set of coils can stimulate a position with a given orientation is easy to compute. This is because this testing can be transformed into solving a convex optimization problem with n variables for each position and orientation, where n is the number of coils, using the convex optimization formulation for single coil from Ref. [21] and interior point method. However, because this computation has to be done for all possible positions and orientations, the utility function is very slow to compute.

In addition to the slow computation, the utility function,

$$utility : \mathbb{R}^{n \times m} \to \mathbb{N} \,, \tag{37}$$

[4] Fermilab neutrino focusing horn, 150 kA pulsed power supply with twenty times the required rise time for TMS, Ref. [42].

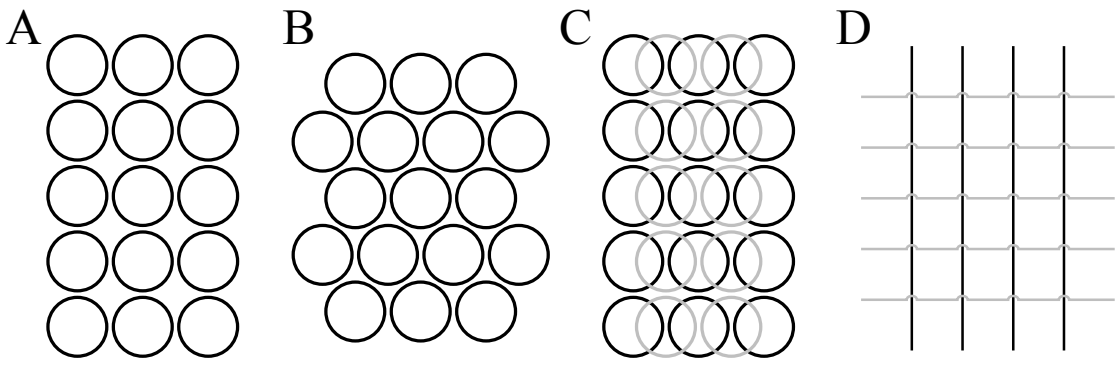

Figure 10: Various proposed mTMS-coil designs. **A** and **B**, square and hexagonal lattices of small circular coils [8, 35]; **C**, partially overlapping small circular coils [34]; and **D**, an array of individual current carrying wires [38].

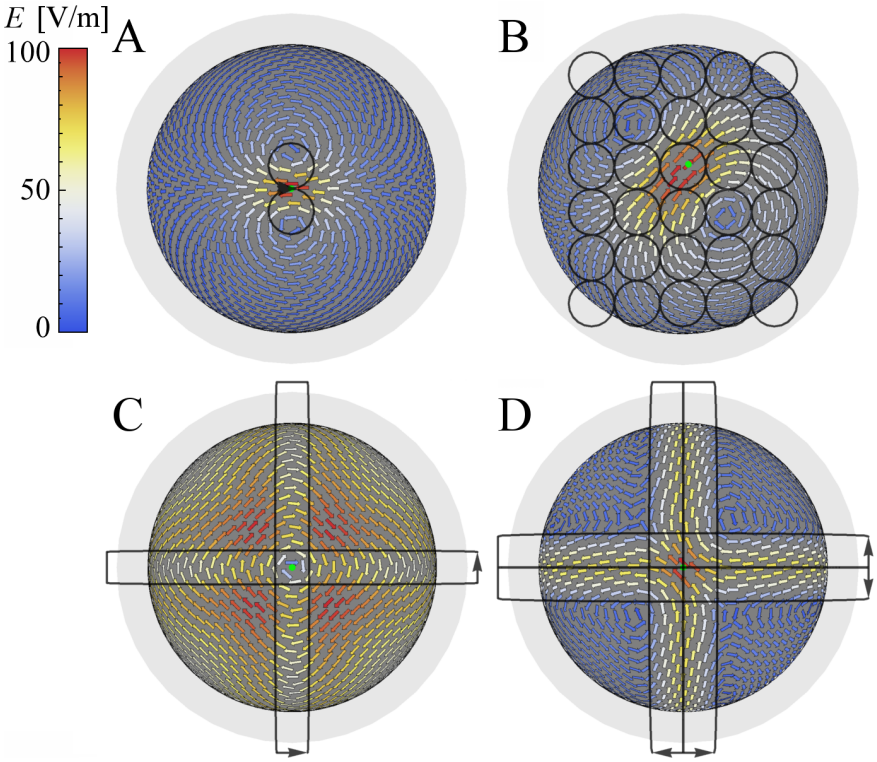

Figure 11: The induced E-fields for four configurations. **A:** a small figure-of-eight coil with 20-mm-diameter circular wings. Total energy of 900 J and 1-turn peak current of 140 kA. **B:** an mTMS device where the coil currents are computed using the optimization method from Section 2.2. Total energy of 250 J and 1-turn peak coil currents between −44 kA and 53 kA (RMS 4.4 kA). **C:** a circular coil approximation with the wire-mesh coil. Total energy of 1100 J and peak current of 50 kA. **D:** a figure-of-eight coil approximation with the wire-mesh coil. Total energy of 2100 J and peak current of 37 kA (twice for the middle wires). These numbers are computed for a 100-V/m stimulus with 50-µs rise-time in spherically symmetric head geometry, where the cortex has radius of 70 mm, and the coil is positioned 20 mm above the cortex, and the wires for wire-mesh coil are 15 mm apart and 280 mm long.

is high-dimensional (n is the number of coils and m is the number of components used to model one coil), and ill-behaved. Unlike for the single-coil optimization, this cost function is non-convex, non-continuous, and non-differentiable.

The high dimensional search space prevents exhaustive search and makes random search ineffective. The non-differentiability prevents using local optimization methods, such as gradient ascension. Thus, solving the problem needs more generic optimization methods. This Thesis tries to solve this optimization problem using differential evolution, which is a generic optimization algorithm designed for continuous input variables [46]. The algorithm mimics biological evolution: there is a population of N sets of n coils, during each time-step each of these sets $\boldsymbol{x}_{\text{existing},i} = [\boldsymbol{c}_{(i,1)}, \ldots, \boldsymbol{c}_{(i,n)}]$, where $\boldsymbol{c}_{(i,k)}$ are individual coils in that set of coils, is mated with a randomly mutated other set of coils from the population,

$$\boldsymbol{x}_{\text{mate},i} = \boldsymbol{x}_{\text{random}} + F \cdot (\boldsymbol{x}_{\text{random}} - \boldsymbol{x}_{\text{random}}) \ , \tag{38}$$

where each $\boldsymbol{x}_{\text{random}}$ presents a randomly selected set of coils from the population, and F is the mutation factor. The mutation factor is typically between 0.4 and 1.0 [47]. In the mating, the new set of coils receives some features from its ancestor and some from the randomly formed mate. This is called crossover, and is controlled by parameter $C \in (0, 1)$.

$$x_{\text{new},i,j} \leftarrow \begin{cases} x_{\text{mate},i,j} \ , & \text{with probability } C \\ x_{\text{existing},i,j} \ , & \text{otherwise} \end{cases} \ , \tag{39}$$

where the index j refers to individual coil components in the coils in that set of coils. This new set replaces the original set $\boldsymbol{x}_i$ only if it is at least as good as its predecessor was. This Thesis applies random scaling for the mutation factor, F, to improve the convergence [47]. This can be achieved by selecting the mutation factor, F, each time uniformly randomly between $1/2$ and 1.

However, the algorithm is not immune to the high dimensionality of the search space. The population size, N, should be larger than the dimensionality of the problem. Typically the population size is ten times the dimensionality [47]. To express a focal TMS coil in spherical geometry requires 63–120 components per coil [21], a number similar to the available degrees of freedom in a MEG signal [24]. This number equals using the 7–10 first degrees (l components) of the spherical harmonic series and their orders (m components, where $m = -l, \ldots, l$).

Because the spherically symmetric geometry has too high dimensionality (a two-coil system equals a 200-dimensional optimization problem), the algorithm was applied to a simplified geometry where the induced E-field shape is expressed using the one-dimensional Fourier series similarly to Section 2.2. This basis requires only 14–20 components per coil to reach similar precision as the 63–120 components per coil would give in the spherical geometry. This basis also reduces the number of possible positions to be tested. However, the latter reduction comes with the cost that only one-dimensional movement of the stimulus position can be tested.

3.2.2 Top-down approach—matrix factorization

The top-down approach begins with the generation of coils that stimulate any point in the desired region in all desired directions. When both position and orientation are discretized, these degrees of freedom can be expressed with N coils. The number of coils should be at least as large as the number of components to express a single coil, m, to avoid overfitting, and the position and orientation must be sampled uniformly to avoid sampling bias. These coils then form a $N \times m$ lead field matrix, $\mathbf{M}$.

The formed lead-field matrix is now N dimensional (number of columns). Dimensionality reduction is applied to this matrix to select n most important linear combinations of the matrix columns.

$$\mathbf{M} \approx \mathbf{FC} \ , \tag{40}$$

where $\mathbf{F}$ is an $N \times n$ matrix of multiplication factors and $\mathbf{C}$ is an $n \times m$ matrix of the coils. Finally, these coils are examined to verify that they offer focal enough stimulus of each point in the desired region. If the coils do not cover the given region, the number of coils is increased or some of the required field positions and orientations are removed; then, the dimensionality reduction procedure is repeated.

Various methods for dimensionality reduction have been studied, and they are applied to a wide range of problems, such as lossy compression of images and video. Some dimensionality reduction methods work by transforming the data into a new basis where individual components are in their order of importance. In this basis, the less-important components can be removed whilst most of the information is retained. For example, in case of JPEG image compression algorithm, this basis is that of discrete cosine series. A general method for finding this kind of basis is the singular value decomposition (SVD).

However, other methods exist offering additional features either for the factors or the coils (Eq. 40). The factors and the coils can be made non-negative (that is, they only have non-negative elements) for a non-negative lead-field matrix (that is, the matrix has only non-negative elements). This kind of factorization was know as self-modeling curve resolution in chemistry [48], positive matrix factorization in data analysis [49], and as non-negative matrix factorization (NMF) in image recognition [50]. However, the basis functions for induced E-field are not naturally non-negative, and thus these methods can not be applied for the lead-field matrix $\mathbf{M}$. In 2010, Ding *et al.* generalized this method for general (not non-negative) matrices [51]. This semi-non-negative matrix (semi-NMF) factorization results in non-negative factors and could help avoiding the limitations caused by asymmetric power electronics (Section 2.4, negative initial voltages are impossible with conventional TMS power electronics).

A convex variant of semi-NMF restricts the coils into convex combinations of the initial coils, which makes the coil-matrix $\mathbf{C}$ sparse [51]. This could be useful when designing an mTMS coil for whole-head coverage. The sparsity has been studied widely for many different matrix factorizations, such as principal component analysis (PCA) and NMF [52, 53, 54]. However, sparseness is not preserved in the change of basis for the coils, and each component in the spherical harmonic basis spans the

whole sphere. Thus, the sparseness for the coils in spherical harmonic series would not equal sparseness in spatial coordinates, and a conversion to spatial basis would be needed. These sparseness constraints suit for example the magnetic-dipole basis, similar to the small circular coils.

Singular value decomposition. SVD is an orthogonal transformation of an $N \times m$ matrix, $\mathbf{N}$, such that

$$\mathbf{N} = \mathbf{U}\mathbf{\Sigma}\mathbf{V}^\top \ , \tag{41}$$

where $\mathbf{U}$ is an $N \times N$ unitary matrix, $\mathbf{\Sigma}$ is an $N \times m$ diagonal matrix of the singular values in descending order, and $\mathbf{V}$ is an $m \times m$ unitary matrix.

Substitution $\mathbf{M} \to \mathbf{N}$ gives an orthogonal representation of the coils ordered by their importance,

$$\mathbf{F} := \mathbf{U} \text{ , and} \tag{42}$$

$$\mathbf{C} := \mathbf{\Sigma}\mathbf{V}^\top \ . \tag{43}$$

The dimensionality reduction is obtained by taking only the first $n \leq \min(N, m)$ rows of matrix $\mathbf{U}$ and columns of matrix $\mathbf{V}$.

Semi-non-negative matrix factorization. Semi-NMF divides an $m \times N$ matrix, $\mathbf{V}$, to two matrices, one of which is non-negative,

$$\mathbf{V} \approx \mathbf{W}\mathbf{H} \ , \tag{44}$$

where $\mathbf{W}$ is an $m \times n$ matrix and $\mathbf{H}$ is an $n \times N$ non-negative matrix (n is an arbitrarily selected parameter for the factorization). The matrices $\mathbf{W}$ and $\mathbf{H}$ are selected such that they minimize the matrix norm of the error,

$$\min ||\mathbf{V} - \mathbf{W}\mathbf{H}||^2 \ . \tag{45}$$

A locally optimal solution to this problem can be found using a gradient descent algorithm:

$$\mathbf{W} \leftarrow \mathbf{V}\mathbf{H}^\top(\mathbf{H}^\top\mathbf{H})^{-1} \ , \tag{46}$$

$$\mathbf{H}_{ik} \leftarrow \sqrt{\frac{(\mathbf{V}^\top\mathbf{W})^+_{ik} + [\mathbf{H}(\mathbf{W}^\top\mathbf{W})^-]_{ik}}{(\mathbf{V}^\top\mathbf{W})^-_{ik} + [\mathbf{H}(\mathbf{W}^\top\mathbf{W})^+]_{ik}}} \ , \tag{47}$$

where operators $\cdot^+$ and $\cdot^-$ divide a matrix $\mathbf{A}$ into positive and negative parts:

$$\mathbf{A}^+_{ik} := (|\mathbf{A}_{ik}| + \mathbf{A}_{ik})/2 \text{ , and} \tag{48}$$

$$\mathbf{A}^-_{ik} := (|\mathbf{A}_{ik}| - \mathbf{A}_{ik})/2 \ . \tag{49}$$

Now, substituting $\mathbf{M}^\top \to \mathbf{V}$ gives the factors and the coils,

$$\mathbf{F} := \mathbf{H}^\top \text{ , and} \tag{50}$$

$$\mathbf{C} := \mathbf{W}^\top \ , \tag{51}$$

where the factors are non-negative. However, the semi-NMF factorization algorithm does not ensure orthogonality of the coils.

3.3 The coil former

This section explains the reader what has been considered when designing the coil former for overlapping TMS coils.

3.3.1 Selecting the material

A TMS coil is subject to extreme Lorentz forces during the stimulus. Ilmoniemi *et al.* estimated this force to be on the order of 10 kN for circular coils [55] by differentiating the expression for magnetic field energy with respect to the coil radius.

The expression for Lorentz force is

$$\boldsymbol{F} = q[\boldsymbol{E} + \boldsymbol{v} \times \boldsymbol{B}] \ , \tag{52}$$

where q is charge, $\boldsymbol{E}$ is electric field, $\boldsymbol{v}$ is the velocity of the charge, and $\boldsymbol{B}$ is magnetic field. The Lorentz force inflicted on a wire is obtained by substituting the electric current, $I = \partial q/\partial t$, and the velocity, $\boldsymbol{v} = \partial \boldsymbol{l}/\partial t$. The force is

$$\partial \boldsymbol{F} = I \partial \boldsymbol{l} \times \boldsymbol{B} \ . \tag{53}$$

If we assume that the wire is perpendicular to the magnetic field and has a diameter d, the pressure between the coil former and the wire is

$$p = \frac{IB}{d} = \frac{10\,\mathrm{kA} \cdot 1\,\mathrm{T}}{1\,\mathrm{mm}} = 10\,\mathrm{MPa} = 100\,\mathrm{bar} \ , \tag{54}$$

where the current and the magnetic field are typical peak values for TMS coil, and the wire diameter has been slightly underestimated compared to that of typical stimulator coils [56].

This pressure lies within the linear part of the stress–strain curve for most plastics. For example, the most common rapid prototyping material (polylactic acid, PLA) has the elastic limit of 50–100 MPa in the TMS timescale [57]. Also, as its Young's modulus for TMS timescale is 2.5 GPa, the PLA will deform less than 0.4%. This calculation suggests that the coil former can be made from most plastic materials. However, because most plastics have a weak maximum tensile strength, the coil former should be encapsulated in a known-to-be-strong case for safety reasons. This can be achieved by laminating the whole coil former inside a thin fiberglass shell, which can withstand the tensile forces. With this design, the coil former material is only subjected to compression.

3.3.2 Selecting the design

Intuitively, an overlapping mTMS coil should be made as thin as possible. This is to minimize the TMS pulse energy (the magnetic field energy) and the heating of the coils. To better understand how important this minimization is, this section first computes the relation between coil–cortex distance and the needed magnetic field energy, and then finds a way to minimize the mTMS coil thickness.

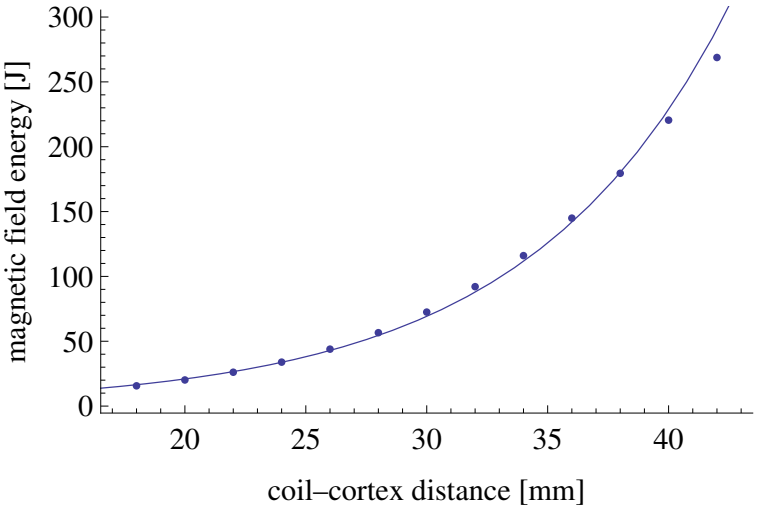

Figure 12: The optimal solution for TMS with 30-mm perpendicular and 50-mm parallel focality, *i.e.*, the full-width half-maximum for induced energy density. The fit is given in Eq. 55.

The relation between coil–cortex distance and the magnetic field energy was computed using the spherically symmetric head model model and the optimization method from Ref. [21]. Fig. 12 shows the minimum-energy solution for distances ranging from 18 to 42 mm, for a 70-mm radius cortex, and with a constant coil focality. The magnetic field energy scales approximately exponentially with the coil–cortex distance z:

$$U(z) = 1.9\,\mathrm{J} \cdot 2^{\frac{z}{5.8\,\mathrm{mm}}} \ . \tag{55}$$

That is, every 5.8 mm increase in the distance doubles the maximum stored energy in the magnetic field and the temperature change in the coil for similar stimulus intensity, as both of these are linearly proportional to the square of the peak current.

A few constraints limit the coil-former thickness. First, to mimic a continuous surface current with discrete wires one needs a coil with multiple loops. Unless each of these coil loops is connected in parallel or in series with long connection wires (Fig. 13) there will be crossing wires. Second, to minimize the coil heating the amount of copper must be maximized in each coil. Thus, there will be little unused space in each coil-former layer, and it is unlikely that a wire crossing could be positioned within the next coil. Thus, for overlapping coils made from one layer of circular wiring, the coil former layer must be at least twice the diameter of the wire[5].

This lower bound can be reached, and an optimal coil-former design is shown in Fig. 14. In this design, the first layer consist of a thin uniform bottom surface, and a layer with thickness equal to the wire diameter. The remaining layers are exactly two wire diameters thick, where the bottom half is reserved for the crossing wires

[5]The mentioned bound applies only to a circular filament. A non-circular filament allows for slightly thinner coil former; however, a non-circular filament is not available in suitably small quantities for a prototype.

from the layer below. For the coil former manufactured for this Thesis, the thin uniform bottom layer is 0.6-mm thick due to manufacturing limitations, and the wire channels have 1.45-mm diameter for housing a 1.25-mm (excluding insulation) copper wire. This wire diameter will be justified later in Section 4.1. The remaining layers are 2.9-mm thick, and the topmost coil in a four-coil coil former lies only 8.7 mm above the bottommost coil.

The coil former was designed using Solidworks 3D CAD, which is a parametric solid model computer-aided design (CAD) program. The modeled coil former was then exported into STL format for 3D printing. The manufactured coil former is shown in Fig. 15. The coil former is 240-mm long and 185-mm wide. A single layer of the coil former is shown in Fig. 16. These coil-former models were relatively complicated to model, as the previously mentioned thickness minimization and wiring-density maximization made them contain lots of partially overlapping wire paths, so called *zero-thickness geometry*, and sharp edges. These problems were fixed by segmenting the cuts into smaller parts, translating problematic wire paths by small amount (0.01 mm), and manually filleting the sharp edges (*fillet* tool, or manual cut when the tool could not solve the resulting geometry), respectively.

3.3.3 Designing a single coil

This section assumes that a desired induced E-field is given, and the target is to design a coil that induces this E-field. This design process has three parts: finding a suitable continuous surface current distribution (in a suitable geometry) that induces the given E-field, discretizing this current distribution into individual coil loops, and joining these coil loops in series.

The continuous surface current distribution inducing an E-field functionally similar to this E-field was computed using the optimization formulation from the TMS-inverse-problem section (Section 2.2), [21]. This Thesis implements restrictions for the area spanned by the surface current to prevent the coils from spanning the opposite side of the head (proposed in Ref. [22]). In addition to these restrictions, the coil were designed with a large 120-mm radius of curvature to ensure that the coils fit the curvature of the human head in most positions. This curvature is a compromise between a tighter 90-mm radius, which would produce more efficient coil as shown in [22], and a flat coil, which can fit against any convex surface. This radius of curvature ensures that the central part of the coil will touch the head surface, minimizing the coil–cortex distance. Fig. 17 illustrates the difference between these three coil shapes.

Similarly to the mentioned studies, the surface current distribution was discretized into current loops using methods described in Ref. [58]. However, this time the number of loops was not a predetermined constant, but was chosen individually for each coil to maximize wiring density. To form a coil, the loops were then connected in series similarly to [58, Fig. 3]. However, this study removed all sharp turns and tight loops from the coil windings with a spatial low-pass filter.

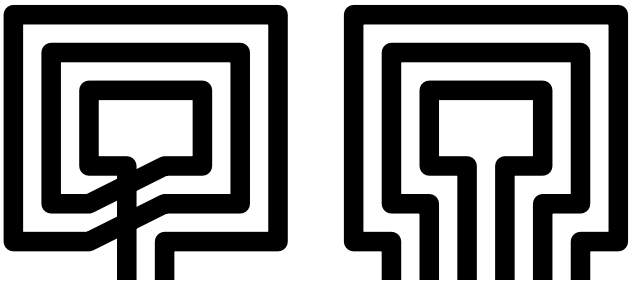

Figure 13: *Left:* Coil loops in series; *right:* coil loops in parallel.

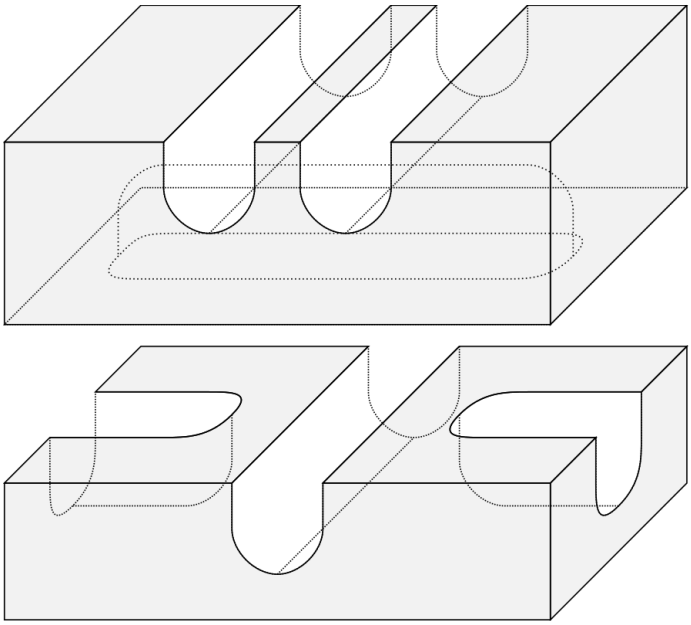

Figure 14: The structure of the mTMS coil former layers. The bottom layer is 2.05-mm thick and the grooves are 1.45-mm deep. The remaining layers are 2.9-mm thick, where the bottom half is reserved for the crossing wires from the lower layer. In addition, all structures with minimum dimension below 0.6 mm are removed, which can be seen in Fig. 16.

Figure 15: The four-coil mTMS coil former. The topmost coil lies just 8.7 mm above the bottommost coil in this four-coil coil former.

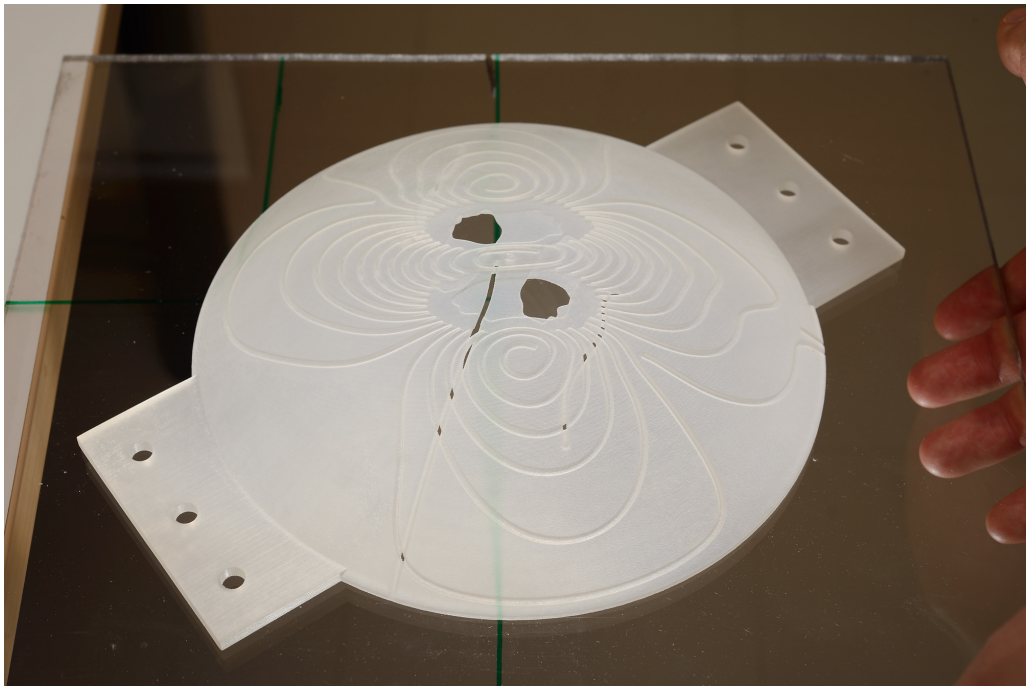

Figure 16: A single layer of the mTMS coil former. The holes in the middle are crafted to ensure that all wiring fits within the layer. The layer has a thickness of 2.9 mm.

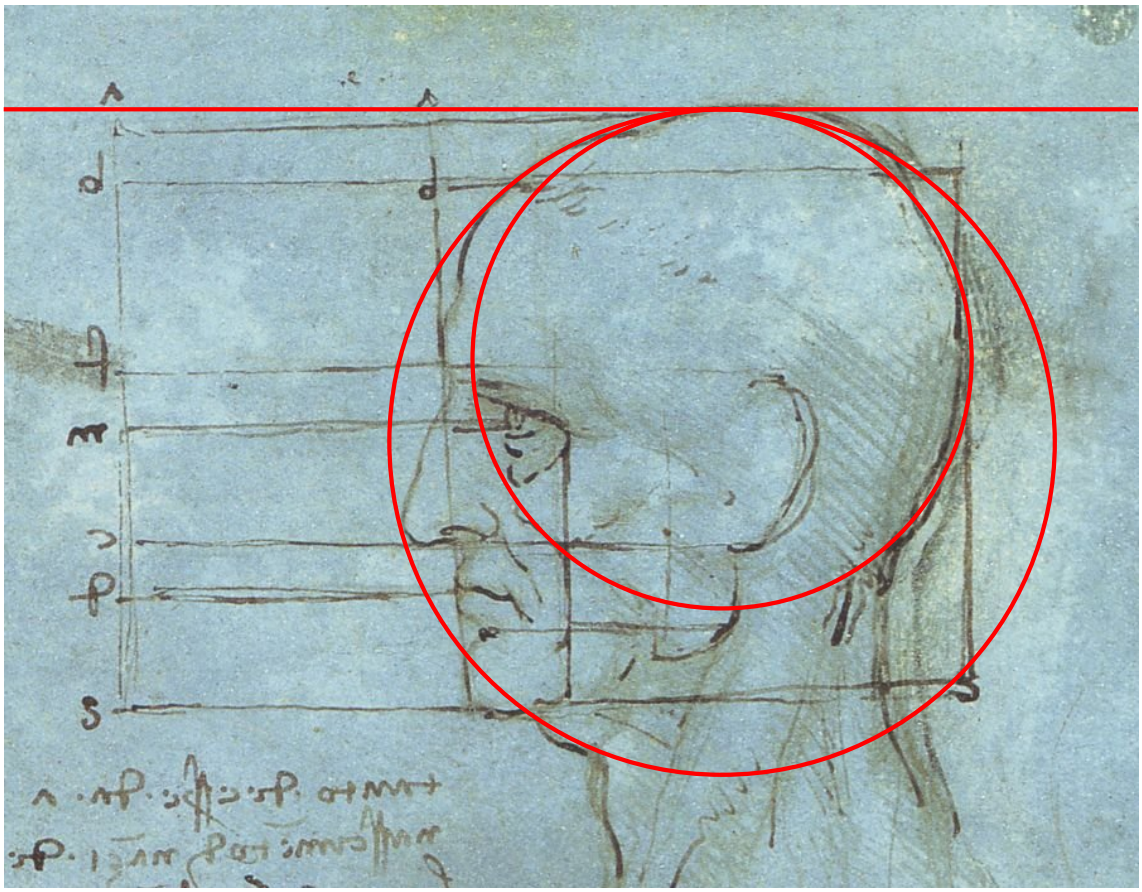

Figure 17: A 90-mm radius sphere, a 120-mm radius sphere, and a planar surface superimposed on the »Proportions of the head» by Leonardo da Vinci. The head size has been scaled to match the 50th percentile (American) adult human male head size from Ref. [59].

3.4 Measurement rig for induced E-field

This section introduces a TMS-induced E-field measurement device that was first presented in Ref. [60]. The device is shown in Fig. 18. It consists of two orthogonal triangular loops that can be rotated to any orientation in the upper hemisphere using two servo motors. These triangle loops have 70-mm radial and 5-mm tangential edges. Thus, the loops measure the two components of the field that would be induced inside a spherically symmetric conductor 70 mm from the origin of the sphere. The triangles form a *triangle phantom* mentioned in Section 2.1.2.

In order to measure the TMS-induced E-field, the TMS coil is connected in series with a known resistor and a signal generator (instead of using TMS-stimulator as the signal source). This allows for high-precision measurement of the coil current, and thus the TMS coil gain. The triangle loops are connected into a preamplifier which is connected to a data-acquisition system. The measurement system has been calibrated by measuring the induced E-field of a custom-built circular coil.

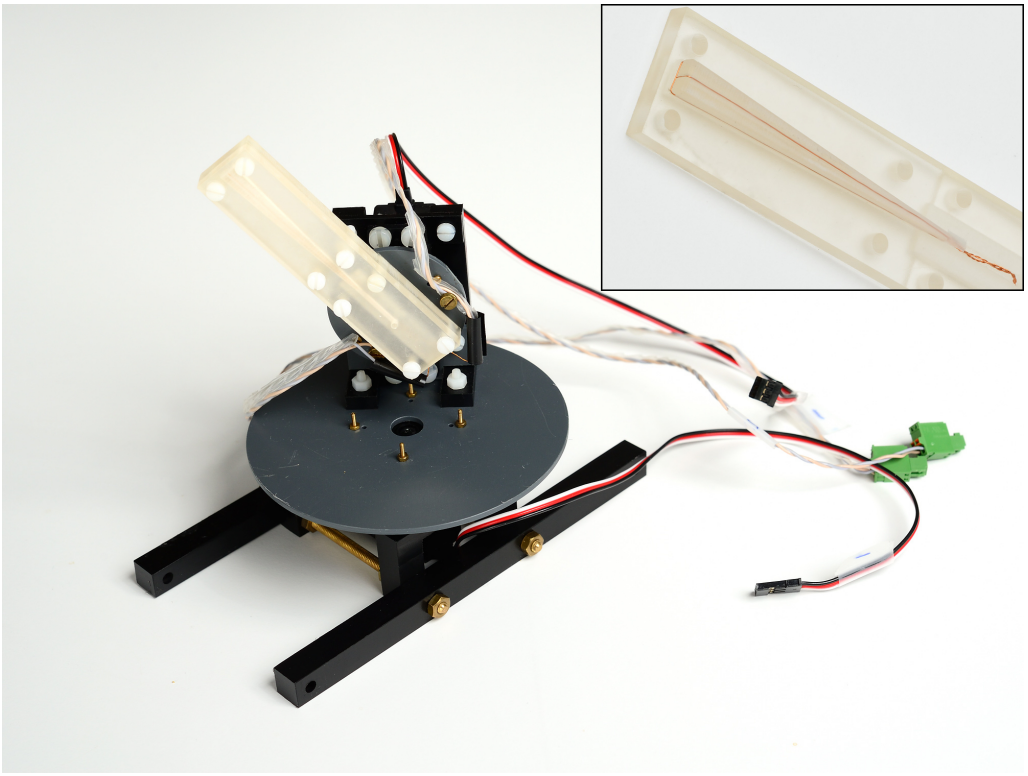

Figure 18: A measurement rig for measuring the induced E-field. The rig has a spatial accuracy of 2.5 mm.

4 Results

The previous chapter introduced methods for mTMS coil design. This chapter will evaluate the coils produced using the methods from the previous chapter. Then, one of the methods is selected, and an experimental mTMS coil is produced from the most promising coil design by that method. This mTMS coil is measured and its inductance and induced E-field is compared to those of simulations.

4.1 Heating of TMS coils

Section 2.3 assumed a normal-conducting TMS coil and gave a formula for computing the approximate temperature rise in a TMS coil (Eq. 30). This section first evaluates using superconducting material for TMS coil and then combines the thinness requirement from Section 3.3 into the previous coil heating results.

The typical wire dimensions for a few TMS coils can be obtained from Ref. [56]. Magstim 70-mm figure-of-eight coil uses a 1 mm × 7 mm rectangular wire, and Medtronic MC-B70 double coil uses 3.5-mm circular wire. These wires have 7 mm^2 and 9.6 mm^2 cross-sectional area, respectively. Thus, the maximum current density is in the order of

$$\frac{10\,\mathrm{kA}}{7\,\mathrm{mm}^2} \approx 1400\,\mathrm{A/mm}^2\ , \tag{56}$$

which is approximately one fifth of the critical current density for most common superconducting materials, like the most commonly used NbTi and Nb_3Sn [61] (at 4.2 K, with magnetic field below 3 T). However, this current density is 1.4 times higher than the common benchmark for superconducting materials, and can not be reached with cheaper-to-use higher-temperature superconducting materials such as MgB_2 at higher temperatures[62].

However, in wire form, the superconductors can not conduct this high current densities. This is because the superconducting wires require a matrix of normal-conducting materials, such as copper. For example, the NbTi wires from Oxford Instruments contain at most 42.5% superconducting material and can reach only 10% higher current density than that of the Magstim coil (at 4.2 K, with magnetic field below 3 T) [63]. In addition, the superconducting coils would require a cryostat moving them a few centimeters farther away from the head, which would increase the required current by at least a factor of two (Fig. 12) making superconducting wires unsuitable for TMS and mTMS.

4.1.1 mTMS-coil wire thickness

The mentioned Magstim and Medtronic TMS coils have coil heating of 0.12 K and 0.07 K, respectively, for a 5-kA peak current 100-µs duration stimulus. However, an mTMS device with overlapping coils should not necessarily use as thick wire as these coils are using. In mTMS coil with 3.5-mm circular wire, the fourth coil would be $3 \times 2 \times 3.5\,\mathrm{mm} = 21\,\mathrm{mm}$ more distant than the first coil. This extra distance would increase the required maximum energy by a factor of 12, based on the distance–power scaling law from Eq. 55. The coil heating would increase to 1 K per pulse, which is

not a major problem. However, the power would increase to 12 times the previous, which would complicate the power electronics significantly.

Noticing that the peak current is proportional to the wire diameter for optimal design, where each coil has maximum number of loops, an approximate scaling law for coil heating is obtained,

$$\Delta T \propto 2^{\left(\frac{1}{2}d_n+\sum_{i=1}^{n-1}2d_i\right)/\lambda_2} / \left(d_n\right)^2 \ , \tag{57}$$

where $\lambda_2 \approx 5.8\,\mathrm{mm}$ is the distance constant for magnetic field energy doubling (Section 3.3.2), n is the index for the coil (counting from the bottom) and d_i is the wire diameter of the i-th coil. Assuming that $d_i = d$ for all coils, the minimum coil heating for a four-coil system is obtained with 2.6-mm wire diameter. The difference in coil heating compared to the 3.5-mm wire diameter is 10% (1.12 prop. unit compared to 1.24 prop. unit). However, the power requirement for the fourth coil is almost halved (6.5 prop. unit compared to 12 prop. unit).

However, by not assuming a constant d_i, the coil heating and the power consumption can be reduced further. Assuming that all coils require similar power in a typical stimulation, the wires in the lower coils should be thinner than those in the upper coils for optimal solution. Coil diameters 2.6 mm, 3.6 mm, 5.9 mm, and 16 mm give relative heating of 0.18 prop. unit. However, the optimum for coil heating is not a good design criterion; with these diameters the topmost coil requires 46 times the power of the lowermost coil. If relative coil heating of 1.12 prop. units is required the optimal coil diameters for minimum power consumption are 1.0 mm, 1.1 mm, 1.3 mm, and 1.5 mm; and the topmost coil has 2.4 prop. unit power consumption.

However, four different coil diameters are too impractical for a prototype. Thus, a 1.25-mm single-strand copper wire, with 0.05-mm polyurethane coating was selected. With this wire the topmost coil has relative heating of 2.0 and relative power consumption of 3.1. This thin wire is relatively easy to bend into complicated shapes required by optimized coil designs and does not need to be Litz wire, as the skin depth

$$\delta = \sqrt{\frac{2}{\omega\sigma\mu}} = 0.92\,\mathrm{mm} \ , \tag{58}$$

where σ is the conductivity of the wire, $\omega = 2\pi \times 5\,\mathrm{kHz}$ is the angular frequency of the current, and $\mu \approx \mu_0$ is the permeability, is larger than the selected wire radius.

4.2 The coils

This section first presents the resulting coil designs obtained using either the bottom-up or top-down approach. Then, a coil design method is chosen. Finally the resulting coils are tested.

The bottom-up design method was tested for one-dimensional problem where the x axis was discretized into 600 equal-spaced points (from $-\pi$ to π) and the utility function was the width of the region near origin that could be stimulated (in points). A stimulus was constrained by requiring the induced energy density to be less than 0.5 times that of the target point in all points more than 15 points from the target point.

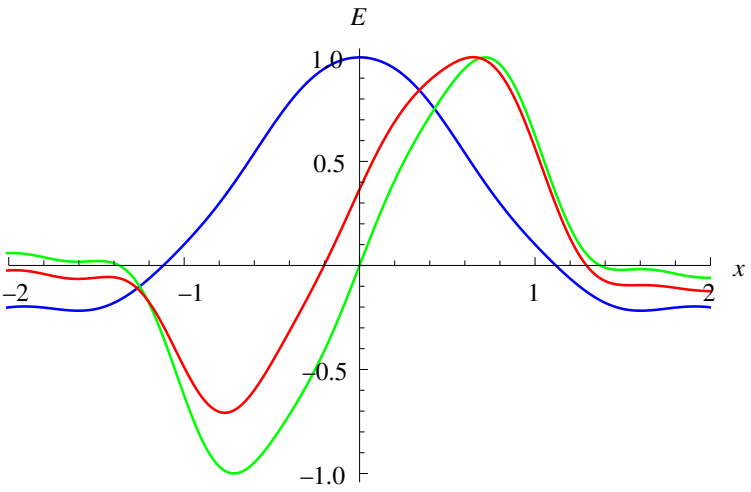

Figure 19: The two induced E-field shapes given by the optimization algorithm. **Blue, coil 1:** a figure-of-eight-coil-like field. **Green, coil 2:** a circular-coil-like field. **Red:** the E-field at the farthest position. These two coils can stimulate any point in the range $x \in [-0.65, 0.65]$, where x axis has been scaled so that the required coil focality is 1 unit.

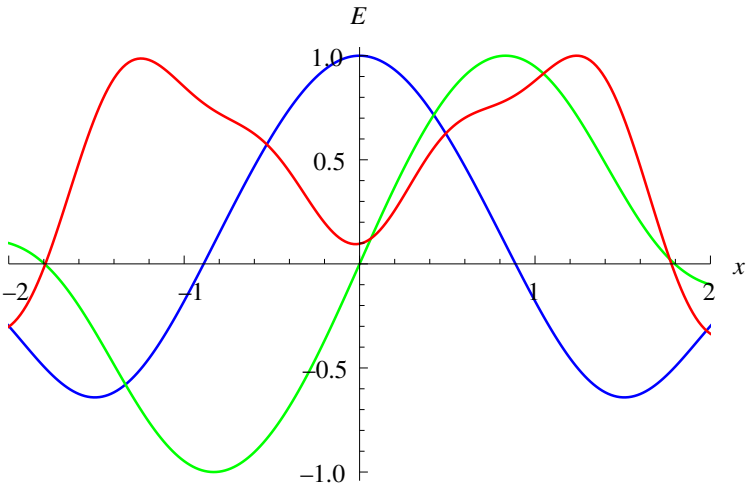

Figure 20: The three induced E-field shapes given by the optimization algorithm. **Blue, coil 1:** a figure-of-eight-coil-like field. **Green, coil 2:** a circular-coil-like-field. **Red, coil 3:** the field of the third coil, the coil does not resemble typical TMS coils. This coil seems to be almost even shaped. These three coils can stimulate any point in the range $x \in [-1.3, 1.3]$, where x axis has been scaled so that the required coil focality is 1 unit.

The first test case was to find the width of the region that can be stimulated with two coils. Having only two coils allowed constraining the first coil to even function (cosine series) and the second coil to odd function (sine series). Also, due to symmetry, the utility function had to be computed only for the positive x axis. These symmetries halved the dimensionality and the computational cost of the utility function.

With 10 components per coil the optimization algorithm converged to a solution in 200 generations, which took 1 h of computation time on a powerful quad-core workstation using Matlab R2013b. However, increasing the number of components used to represent each coil from 10 to 15 prevented finding the solution (with random initialization) in a reasonable time. A smarter initialization, using the previously found 10-component solution as the basis for initial guess, converged but did not improve the optimal solution significantly. Thus, this study revealed that with two coils the stimulus location can be moved in an area 1.3 times wider than the focality of a single coil (defined as the full-width half-maximum for the induced energy density). The optimal induced E-fields are shown in Fig. 19.

The second test case was to find the width of region that can be stimulated with three coils. Unlike with two coils, the third coil is not necessarily either even or odd function. Thus, the third coil had both cosine and sine components and the utility-function-computation could not be limited to only the positive x axis.

Adding the third coil made the utility-function evaluation more expensive for at least two reasons: more points need to be evaluated each time (as the solution has much larger coverage) and testing for failure is much slower for three variables than for two variables for each point. Thus, the optimization did not converge with several days of computation and over 500 generations. However, even though the system had not converged into an optimal solution, the best found solutions for the three-coil problem could stimulate much broader area than the two coil solutions. The best solution found could stimulate an area 2.6 times wider than the coil focality (Fig. 20).

The bottom-up solution does, however, have one apparent problem in addition to the performance issue. As the coil–cortex coupling is not optimized, coils producing the resulting induced E-fields shapes are expensive in terms of energy. Using the constrained-optimization-formulation method from Section 2.2 does not improve this situation because the induced E-field shapes have large spatial derivatives that must be preserved for a working solution (near $|x| = 1$ in the second coil in Fig. 19 and near $|x| = 1.5$ in the third coil in Fig. 20).

The top-down design method has the potential to fix the problems associated with the bottom-up method. First, the top-down method can compute any number of coils in the same time. Second, because the initial set of coils can be made to contain only optimized (in terms of energy) coil designs, the resulting coils will be highly effective (at least when using a convex matrix factorization). However, unlike the bottom-up solution, the top-down solution is not guaranteed to be able to stimulate all points in the desired region.

This Thesis considers only an mTMS device with a few channels. This simplifies the coil design and construction, as the coil covers only a small proportion of the

head. Thus, the induced E-field can be computed using spherical head model and all designed coils can be stacked on top each other. Thus, there is no need for sparse matrix factorization.

The coils to stimulate each position and orientation could be optimized by using the method described in Ref. [21]. However, computing the optimization constraints (*i.e.*, the lead field) takes almost 10 s and the actual coil optimization with 440 variables takes 1–10 s on a workstation computer. Thus, computing the optimal coil for each position and orientation would take several hours (assuming approximately 1000 positions and orientations). This would slow down exploring the number of coils needed for a given set of positions and orientations. However, the spherical harmonics used to express the coils in spherically symmetric geometry can be rotated with closed-form rotation matrices [64]. With these matrices a rotation takes 0.1 s, which is two orders of magnitude faster than the coil optimization. This allows exploring different sets of positions and orientations, which allows for finding the degrees of freedom for an mTMS system with a few channels.

4.2.1 Degrees of freedom in mTMS-induced E-fields

This section describes the found degrees of freedom with each number of coils. These results were obtained by performing SVD to the matrix of possible coils and selecting the n most important coils. Most of these are *trivial*; however, surprisingly only five coils are required for full range of small position and orientation corrections. The expected number of necessary coils is six: three for controlling the horizontal-direction field maximum (strength, and position in horizontal and vertical direction) and three for controlling the vertical-direction field maximum. The results are described below and then summarized in Table 2.

Two coils. There are three distinct two-coil systems: one allowing all orientations, one allowing small shift in the direction perpendicular to the induced E-field maximum and one allowing small shift in the parallel direction.

Three coils. Three coils allow for combining small movement in one direction and a partial orientation control. The partial control results from fixed position for the induced E-field maximum in one of the two directions. Three coils do not seem to allow position control in a region with constant induced E-field direction. Rather, the direction of the maximum induced E-field will change when moving to directions that are neither parallel nor perpendicular with the original induced E-field. However, even if such a solution exists, it would be sensitive to non-sphericality of the human head.

Four coils. Four coils allow for controlling the field position in a small region with limited position control. Similar to the three-coil case, the position control is reduced when the field is far from the original induced E-field direction.

Five coils. Five coils allow for all induced E-field orientations inside a small region. The sixth coil is not needed for covering a small region in all directions because a circular coil can produce a movement perpendicular to the induced E-field direction regardless of this direction.

When SVD is replaced with semi-NMF, coils requiring only positive initial current

Table 2: A sketch of the coil designs obtained for 2–5-orthogonal-coil mTMS device using the top-down approach. The resulting coils can be divided into circular, figure-of-eight, and clover-leaf coil shapes. The coils are in order of their importance for the system; however, this order is not unique for sets capable of stimulating all directions. Counter-clockwise windings are in red and clockwise windings in black. The coils are displayed in an azimuthal equidistant projection.

coils	position	orientation
	one point	all directions
	a vertical line segment	horizontal
	a horizontal line segment	horizontal
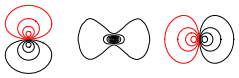	a vertical line segment	near horizontal
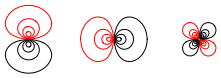	a vertical line segment	near horizontal
	a small region	near horizontal
	a small region	all directions

Table 3: A sketch of the coil designs obtained for four unidirectional-current coil mTMS device using the top-down approach. Counter-clockwise windings are in red and clockwise windings in black. The coils are displayed in an azimuthal equidistant projection.

coils	position	orientation
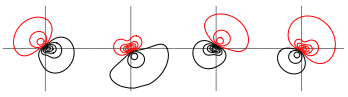	a small region	near horizontal, pointing left

directions are obtained. The resulting coils are figure-of-eight-like coils that have been shifted and twisted. The number of coils to obtain the positional degrees of freedom for the induced E-field are similar to the coils produced using SVD. However, to obtain free coil orientation required three coils instead of two coils. The four-coil system for a small region with limited directions with non-negative currents is shown

in the Table 3. These coils have mutual inductance coupling coefficients between -0.3 and 0.3. The negative coupling coefficients limit the possible range of movement using positive initial voltages because of Eq. 36.

4.2.2 The selection of an mTMS coil

This Thesis selected a set of four coils for the prototype mTMS coil. This selection was made because four coils allow for fine tuning both the stimulus position and the stimulus orientation without physically moving the coil. That is, four is the smallest number of coils offering apparent gains from a multichannel design. However, the coils in Tables 2 and 3 span almost the whole head. Thus, they are unsuited for TMS as they can not be placed against the head surface outside the top of the head. Because of this, and a limitation in coil-former manufacturing technique (maximum coil-former diameter in one direction 185 mm) the selected coils were designed to have a 120-mm radius of curvature and a maximum diameter of 185 mm, which is 20% larger than the circular coil at the last row in Table 2.

The coil size is still significantly larger than the desired position degree of freedom, so this size limitation does not affect the position control. However, with this limitation in place, the mutual coupling of semi-NMF coils was increased to range between -0.8 and 0.3. The high negative coupling coefficients would either limit the possible movement significantly or require negative voltages in power electronics removing the desired unidirectionality. Because of this, a set of four orthogonal coils found using SVD were selected. These coils are shown in Fig. 21.

4.3 The selected mTMS coil

A minimum-thickness coil former was manufactured for the selected coils using methods from Section 3.3. Thus, the first coil is 0.6 mm above the bottom surface of the coil former, and the coils have a spacing of 2.9 mm between them.

With these coil spacings, the inductance matrix, $\mathbf{L}$, was computed.

$$\mathbf{L} = \begin{bmatrix} 10.5 & 0.001 & -0.007 & -0.007 \\ 0.001 & 10.5 & 0.08 & -0.06 \\ -0.007 & 0.08 & 9.8 & -0.2 \\ -0.007 & -0.06 & -0.2 & 10.0 \end{bmatrix} \mu\text{H} \ , \tag{59}$$

where the diagonal elements are the coil inductances and the off-diagonal elements are the mutual inductances between the coils. The magnitude of the mutual inductances is more obvious when this inductance matrix is transformed into coupling coefficient form:

$$k_{ij} = \frac{L_{ij}}{\sqrt{L_{ii} L_{jj}}} \ , \tag{60}$$

$$\mathbf{k} = \begin{bmatrix} 1 & 0.0001 & -0.0007 & -0.0007 \\ 0.0001 & 1 & 0.008 & -0.006 \\ -0.0007 & 0.008 & 1 & -0.02 \\ -0.0007 & -0.006 & -0.02 & 1 \end{bmatrix} . \tag{61}$$

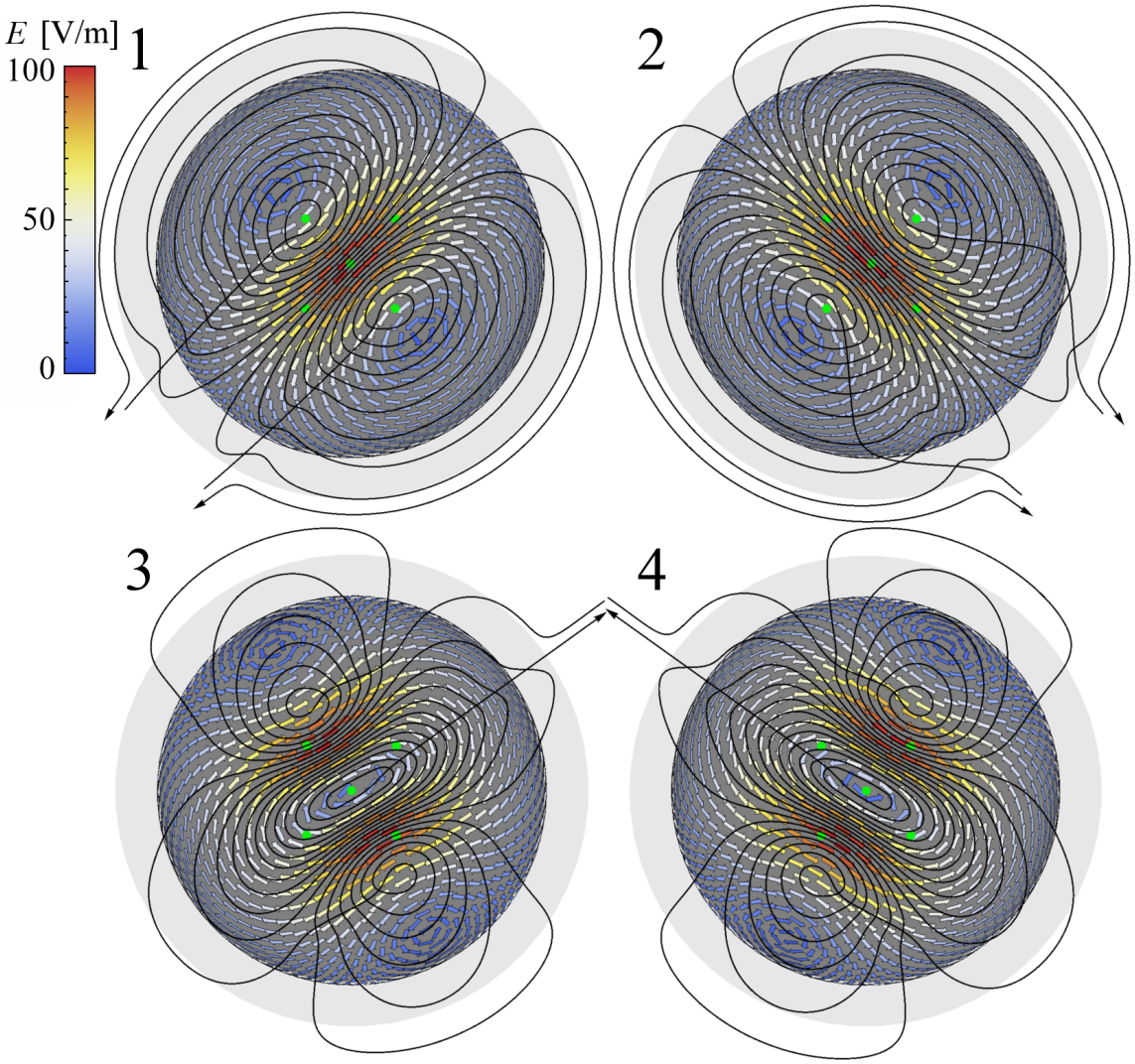

Figure 21: A set of four coils similar to the penultimate row in Table 2. However, the coils have different radius of curvature, a limited diameter, and they are a orthogonal linear combination where the first and the third coil and the second and the fourth coil have been combined into sum-and-difference pairs (1 and 2, 3 and 4, respectively). The figure shows also the computed values for TMS-induced E-field at the cortex when the cortex radius is 70 mm and the minimum coil–cortex distance is 20 mm (for the coil former).

Because the off-diagonal elements have absolute value significantly smaller than unity, the coils are almost orthogonal.

A coil has both resistance and inductance (and negligible capacitance). Thus, its impedance is

$$Z_{\text{coil}}(\omega) = R + i\omega L \ , \tag{62}$$

where R is its resistance, ω is the angular frequency, L is its inductance, and $i = \sqrt{-1}$. The impedance describes the ratio between voltage, V, and current, I,

$$V = ZI \ . \tag{63}$$

The easiest way to measure the coil inductance is to measure the impedance at different angular frequencies. To do this, the coil was connected in series with a known resistor ($R = 12.1\,\Omega$) and a signal generator.

The most accurate measurement would be obtained by measuring the impedance at several angular frequencies and fitting a linear regression. However, a sufficient accuracy is obtained by using only two frequencies: almost direct current (50 Hz) and a similar to TMS-pulse characteristic frequency (10 kHz). Now,

$$\operatorname{Re} Z_{10\,\text{kHz}} \approx Z_{50\,\text{Hz}} \ , \text{ and} \tag{64}$$

$$\operatorname{Im} Z_{10\,\text{kHz}} \approx \sqrt{(Z_{10\,\text{kHz}})^2 - (Z_{50\,\text{Hz}})^2} \ . \tag{65}$$

Substituting the values from Tables 4 and 5, the inductances shown in Table 6 are obtained. The measured inductances are between 1.1% and 2.3% above the computed values.

The mutual inductances were measured by connecting the coil to be measured in series with an oscilloscope. Because the oscilloscope has a high internal resistance, the current in the measured coil is essentially zero and only one data point is needed to obtain the mutual inductance. However, to ensure that the measured voltage is due to mutual inductance (*i.e.*, it has opposite phase to the coil current) the voltage over the resistor was measured simultaneously. Because of crosstalk between the channels, the oscilloscope had a root-mean-square (RMS) noise of 3 mV, which prevented measuring mutual inductance below 0.2 µH. The measured absolute values for coupling coefficient were

$$|\mathbf{k}| = \begin{bmatrix} & < 0.02 & < 0.02 & < 0.02 \\ < 0.02 & & < 0.02 & < 0.02 \\ < 0.02 & < 0.02 & & \approx 0.04 \\ < 0.02 & < 0.02 & \approx 0.04 & \end{bmatrix} \ , \tag{66}$$

which suggest that the coils are almost orthogonal, with the mutual inductance between coils 3 and 4 slightly larger than the other mutual inductances, similarly to the computed coupling coefficients (Eq. 61).

In order to measure the induced E-field, the mTMS coil was placed above the measurement device from Section 3.4. The coil position had approximately 5-mm uncertainty in horizontal direction and 1-mm uncertainty in the more important

Table 4: The measurement data at 50-Hz frequency. The numbers are peak-to-peak values averaged over 1000 trigger events.

coil	V_{resistor} [V]	I [A]	V_{coil} [V]	$\lvert Z_{\text{coil}}\rvert$ [Ω]
1	3.832	0.317	0.0358	0.113
2	3.834	0.317	0.0287	0.0907
3	3.812	0.315	0.0258	0.0820
4	3.835	0.317	0.0264	0.0832

Table 5: The measurement data at 10-kHz frequency. The numbers are peak-to-peak values averaged over 1000 trigger events.

coil	V_{resistor} [V]	I [A]	V_{coil} [V]	$\lvert Z_{\text{coil}}\rvert$ [Ω]
1	3.780	0.312	0.214	0.686
2	3.844	0.318	0.217	0.683
3	3.845	0.318	0.200	0.628
4	3.844	0.318	0.205	0.644

vertical direction (the orientation had a 1° uncertainty). These measurements were performed at two different coil-former–cortex distances 15 mm and 20 mm. The measured field shapes are similar to the computed field shapes, which can be seen by comparing the computed fields (Fig. 21) to the measured fields (Fig. 22). The maximum field magnitudes are shown in Tables 7 and 8. The measured maximum field magnitudes differ −3–9% from the computed field magnitudes. The average error in these magnitudes can be explained by the 1-mm uncertainty in the coil–cortex distance (which can be computed to cause 5–6% difference in the field magnitude, and a negligible difference in the field shape). The reason for inter-coil variation could be due to the asymmetric coil-position in relation to the measurement rig, which can be estimated to have been 3 mm for both measurements (but in different directions), or to the (low) density of measurement points not finding the exact maximum field magnitudes.

The measured E-field exhibits the desired degrees of freedom. A linear combination of the four coils can can move the stimulus maximum into any point in a 30-mm-diameter region with the orientation ranging from −15° to 15° degrees from the horizontal direction (i.e. the direction between the two handles in the coil former). However, the energy cost of a stimulus varies with position. If a a 50-µs rise-time 100 V/m stimulus is assumed, the maximum stored energy varies from below 40 J in the central region to over 200 J (maximum translation in diagonal direction with maximum orientation change). Most positions and orientations do not require currents above 5000 A. Tables 9 and 10 show some linear combinations along with the respective maximum currents and maximum magnetic field energy.

Table 6: The self-inductances for the coils.

coil	Re Z [Ω]	Im Z [Ω]	L_{measured} [µH]	$L_{\text{simulated}}$ [µH]
1	0.113	0.677	10.8	10.5
2	0.0907	0.677	10.8	10.5
3	0.0820	0.623	9.91	9.80
4	0.0832	0.639	10.2	10.0

Table 7: The peak value for the TMS-induced E-field when the coil former is located 15 mm above the cortex.

coil	computed E-field $\left[\frac{\text{µV/m}}{\text{A/s}}\right]$	measured E-field $\left[\frac{\text{µV/m}}{\text{A/s}}\right]$
1	2.54	2.55
2	2.20	2.11
3	0.90	0.90
4	0.76	0.70

Table 8: The peak value for the TMS-induced E-field when the coil former is located 20 mm above the cortex.

coil	computed E-field $\left[\frac{\text{µV/m}}{\text{A/s}}\right]$	measured E-field $\left[\frac{\text{µV/m}}{\text{A/s}}\right]$
1	1.98	2.06
2	1.72	1.70
3	0.65	0.67
4	0.56	0.53

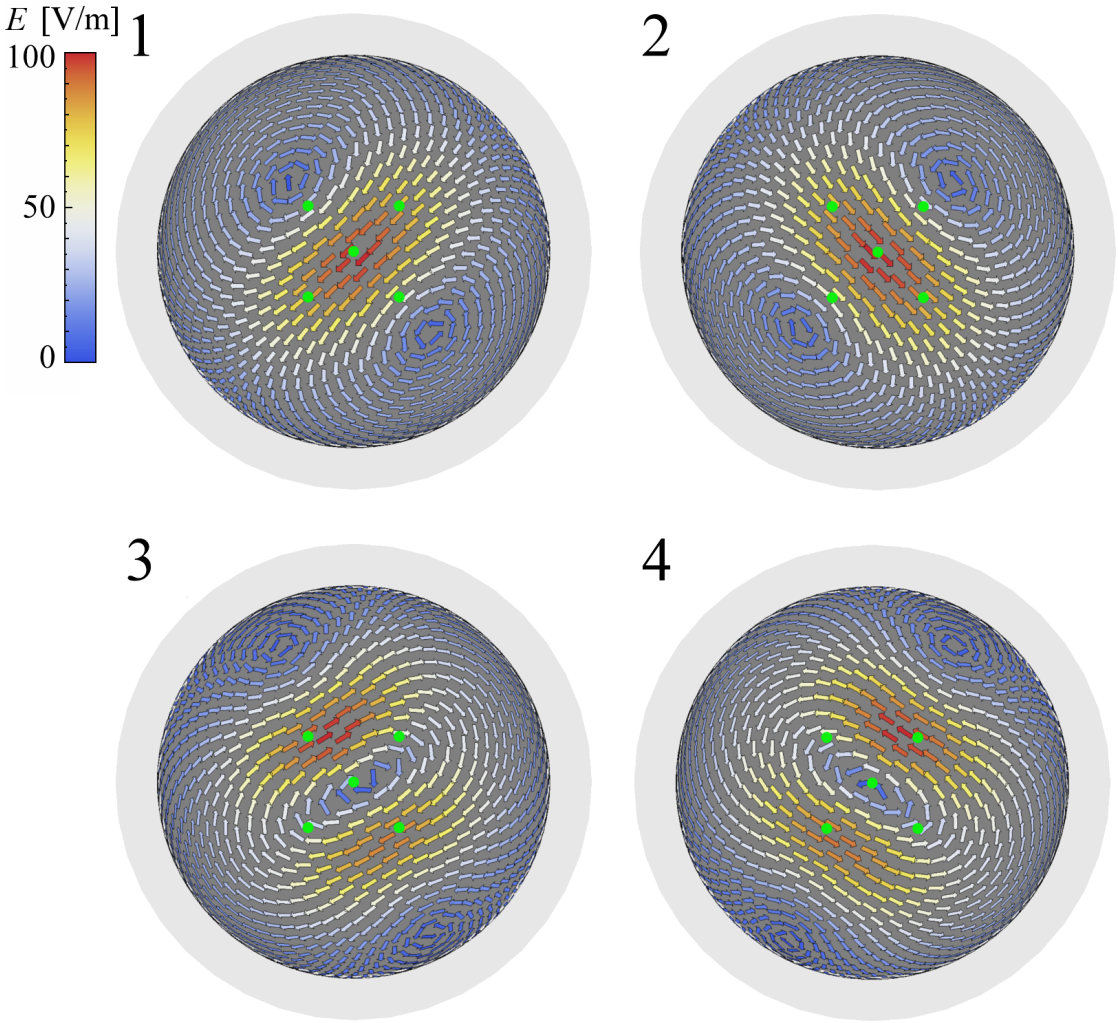

Figure 22: The measured induced E-field pattern at 20 mm coil–cortex distance. Because the other measurement (at 15-mm coil–cortex distance) had opposite asymmetry as this measurement, the asymmetry in these fields is most likely due to the coil position not being exactly in the middle, not asymmetry in the coils. If we assume that the coil formers are symmetric, the coil former is approximately 3 mm south-east from the center.

Table 9: Some possible induced E-field maximum positions and orientations with respective magnetic field energies, U, and maximum currents, $\boldsymbol{I}$.

induced E-field	U [J]	$\boldsymbol{I}$ [A]	induced E-field	U [J]	$\boldsymbol{I}$ [A]
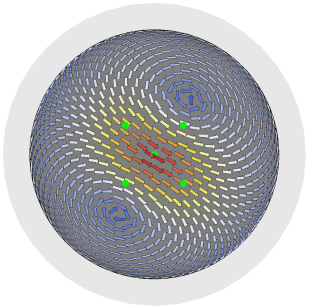	45	$\begin{bmatrix} 590 \\ 2900 \\ 0 \\ 0 \end{bmatrix}$	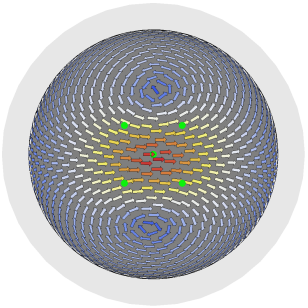	38	$\begin{bmatrix} 1700 \\ 2100 \\ 0 \\ 0 \end{bmatrix}$
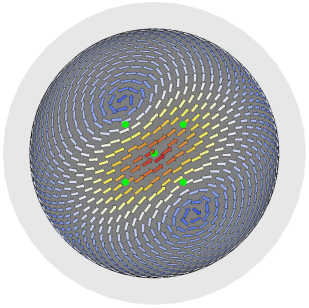	31	$\begin{bmatrix} 2400 \\ 440 \\ 0 \\ 0 \end{bmatrix}$	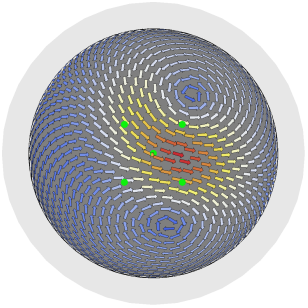	120	$\begin{bmatrix} 960 \\ 2300 \\ -2500 \\ -3400 \end{bmatrix}$
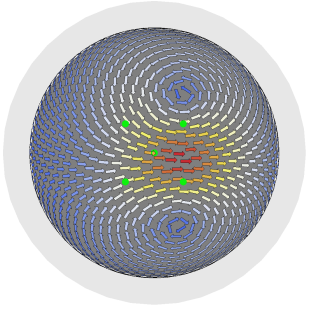	100	$\begin{bmatrix} 1500 \\ 1900 \\ -2600 \\ -2600 \end{bmatrix}$	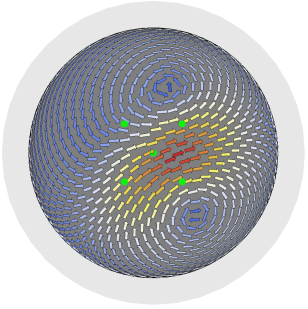	120	$\begin{bmatrix} 2100 \\ 740 \\ -2800 \\ -3200 \end{bmatrix}$
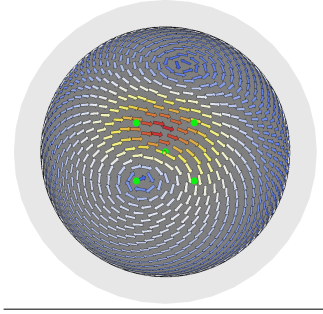	110	$\begin{bmatrix} 510 \\ 1900 \\ 3000 \\ -3000 \end{bmatrix}$	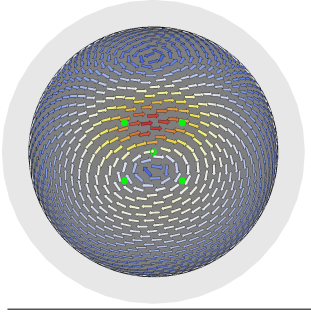	170	$\begin{bmatrix} 710 \\ 870 \\ 4000 \\ -4000 \end{bmatrix}$
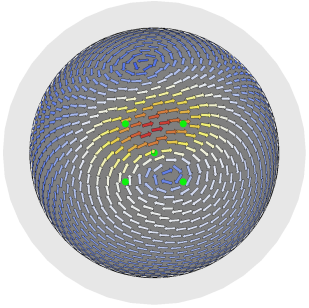	130	$\begin{bmatrix} 1300 \\ 610 \\ 3400 \\ -3500 \end{bmatrix}$	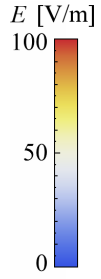		

Table 10: Some possible induced E-field maximum positions and orientations with respective magnetic field energies, U, and maximum currents, $\boldsymbol{I}$.

induced E-field	U [J]	$\boldsymbol{I}$ [A]	induced E-field	U [J]	$\boldsymbol{I}$ [A]
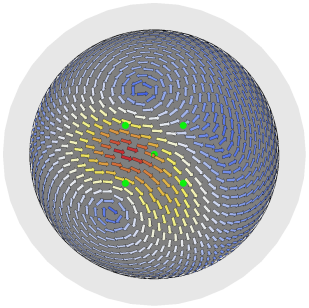	150	$\begin{bmatrix} 650 \\ 2400 \\ 3200 \\ 3700 \end{bmatrix}$	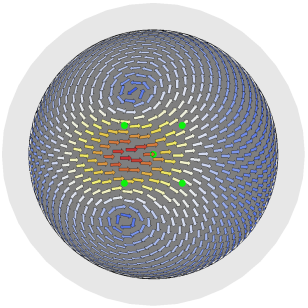	100	$\begin{bmatrix} 1500 \\ 1900 \\ 2600 \\ 2600 \end{bmatrix}$
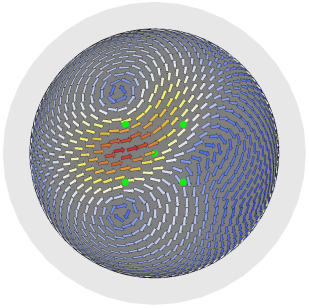	190	$\begin{bmatrix} 1400 \\ 1100 \\ 4700 \\ 3700 \end{bmatrix}$	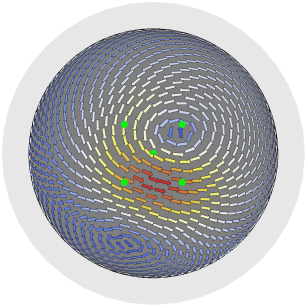	120	$\begin{bmatrix} 420 \\ 2000 \\ -3100 \\ 3100 \end{bmatrix}$
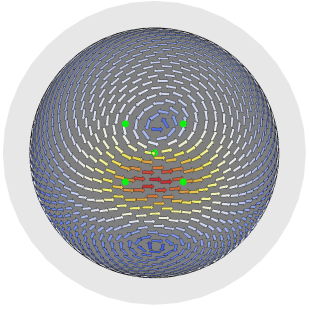	100	$\begin{bmatrix} 1300 \\ 1500 \\ -2900 \\ 2700 \end{bmatrix}$	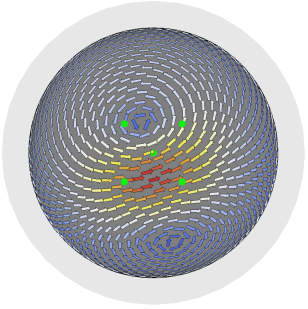	80	$\begin{bmatrix} 1900 \\ 1000 \\ -2300 \\ 2300 \end{bmatrix}$
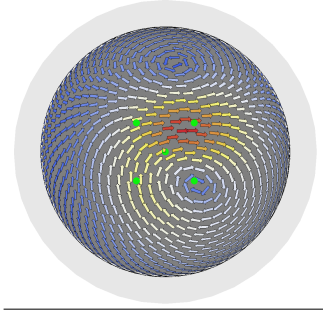	190	$\begin{bmatrix} 1600 \\ 440 \\ 760 \\ -5800 \end{bmatrix}$	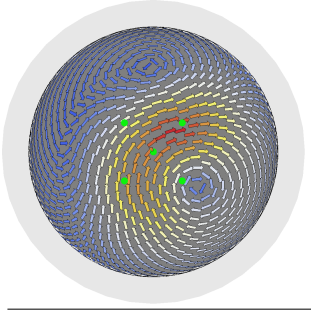	170	$\begin{bmatrix} 2200 \\ -330 \\ 0 \\ -5500 \end{bmatrix}$
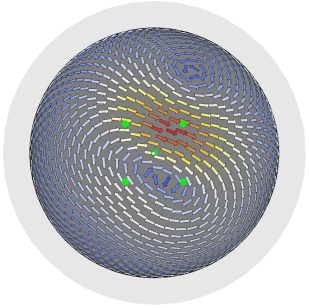	240	$\begin{bmatrix} 670 \\ 1200 \\ 270 \\ -6700 \end{bmatrix}$	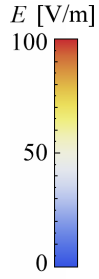		

5 Discussion

This Thesis proposes a novel design for mTMS. This design, large thin overlapping coils, was motivated by several difficulties in previous mTMS designs based on small periodic coil lattices. These difficulties included three major design problems: trade-off between power requirements and positional accuracy, high currents and heating of the small coils, and high number of channels required for covering large areas. The proposed design tries to address the first two of these problems. This chapter evaluates whether these problems were eliminated.

Chapter 2 introduced the TMS-induced E-field inverse problem in Section 2.2. A good solving method for this problem is required to reduce the power requirements and coil heating for an mTMS device. This solving method is required for both designing the mTMS device and operating it. Section 2.2 figured that a good solution for this problem can be found using either Tikhonov regularization or the constrained optimization formulation from Ref. [21].

Chapter 3 presented two different methods for generating the large thin mTMS coils. The first method expressed the maximizing induced E-field position and orientation control as an optimization problem. However, no sufficiently fast solver was found for this optimization problem. The second method expressed the coil design as a dimensionality reduction, for which exists multiple efficient solvers. This method was used in Chapter 4 to design an mTMS coil with four large thin overlapping coils.

Using the single coil optimization method from Ref. [21], this Thesis found an empirical scaling law for the maximum stored magnetic field as a function of coil–cortex distance, z,

$$U(z) \propto 2^{z/\lambda_2} \ . \tag{67}$$

where $\lambda_2 \approx 5.8\,\text{mm}$ for coil–cortex distances between 15 mm and 35 mm. The exponential scaling with such a small *distance constant* complicates the overlapping coil design. Because of this, the coils must be made from relatively thin wire, which causes larger coil heating. And, as the coil heating is proportional to the inverse square of the cross-sectional area, enlarging the wire diameter reduces coil heating for thin wires but requires more stimulation power to operate; for thick wires, such as those used in TMS coils, reducing wire diameter both reduces the coil heating and power consumption.

The top-down method for overlapping mTMS coil design was presented and tested. The method, including translating continuous surface current distribution into an actual coil, works very well. The designed coils have the specified position and orientation degrees of freedom, they have almost zero mutual inductance if desired, their self-inductances are very close to expected values, and their induced E-field has the expected shape and gain. Thus, this Thesis claims that large thin overlapping coils offer a practical approach for mTMS.

This Thesis evaluated each coil design using a 100-V/m stimulus with 50-µs rise-time. This stimulus requires one-half the current, and thus, one-fourth the energy of a 100-V/m stimulus with 100-µs rise-time. For the reference, a conventional figure-of-eight coil requires approximately 80 J of energy for this stimulus, and the optimal single-coil design requires only 20 J [21]. These stimuli have mean stimulus

power of 1.6 MW and 0.4 MW, respectively. This Thesis estimates, that a stimulator using a lattice of 20-mm circular coils requires at least 250 J for a focal stimulus, which equals 5.0 MW mean stimulus power; an order of magnitude more than a single-coil TMS device. However, this figure only applies near the center of the lattice. With the proposed large thin overlapping coils, the stimulus energy for a focal stimulus was from 30–50 J (different orientations near the central region) to 100–240 J (different orientations near the maximum displacement). These stimuli require from 0.6–1.0 MW to 2.0–4.8 MW mean stimulus power, respectively, which is a significant improvement compared to the small-circular-coil design.

The reduction in required mean stimulus power suggests that the concept of large thin overlapping coils works. However, the large variation in this power requirement reveals that there are several things that could be enhanced. The expected power requirement could be reduced by re-ordering the coils. Because the E-field induced by two topmost coils (used to translate the induced E-field position) decays faster with distance than that of the two lowermost coils (Tables 7 and 8), these two topmost coils should be moved below the two lowermost figure-of-eight coils. Also, the two figure-of-eight coils should be rotated by 45° so that the lower coil would became a more used component (which is equal to not performing the orthogonal mixing for the figure-of-eight coils).

The mTMS design method presented in this Thesis is a significant step towards a working mTMS device. The described coil-optimization methods can be used also for other mTMS design concepts than the large thin overlapping coils. However, even with these methods, building an mTMS device will not be easy: the coil heating issue has been mitigated, not eliminated; and thus unless major improvements are found, performing rTMS with an mTMS device will be a major challenge.

6 Conclusion

This Thesis presented a novel design concept for mTMS, large thin overlapping coils. The developed design allows for significantly smaller power consumption and number of channels (for stimulating a small region) than the previous designs. These improvements allow for constructing a practical mTMS device, which was demonstrated by building a prototype mTMS coil. The prototype was measured to require smaller stimulation pulse energy than a conventional figure-of-eight coil whilst allowing for position correction in an area with 15-mm diameter. Higher energies allowed for a position correction in an area with 30-mm diameter. This design concept is a major step towards a fully functional mTMS device.

The presented mTMS coil offers small position and orientation corrections. Such a coil can be used for example for easier motor-cortex mapping or more accurate stimulation of a specific target. Both of these could be performed by placing the coil roughly above the target region and letting the control software do the finer position and orientation control. This would likely reduce the total error between the desired stimulus site and the true stimulus site.

mTMS seems to be a major improvement to TMS in several applications. An mTMS coil with just four channels can perform small position and orientation corrections which may improve the accuracy of, for example presurgical mapping. In addition to this, an mTMS device can produce new types of stimuli, such as paired-pulse TMS with different pulse positions. The new types of stimuli can reveal more about brain functionality.

References

[1] J. Ruohonen and J. Karhu. Navigated transcranial magnetic stimulation. *Neurophysiologie Clinique/Clinical Neurophysiology*, 40(1):7–17, 2010.

[2] A. T. Barker, R. Jalinous, and I. L. Freeston. Non-invasive magnetic stimulation of human motor cortex. *Lancet*, 325(8437):1106–1107, 1985.

[3] A. T. Barker, I. L. Freeston, R. Jalinous, and J. A. Jarratt. Clinical evaluation of conduction time measurements in central motor pathways using magnetic stimulation of human brain. *Lancet*, 327(8493):1325–1326, 1986.

[4] S. Ueno, T. Tashiro, and K. Harada. Localized stimulation of neural tissues in the brain by means of a paired configuration of time-varying magnetic fields. *Journal of Applied Physics*, 64(10):5862–5864, 1988.

[5] J. P. Brasil-Neto, L. G. Cohen, M. Panizza, J. Nilsson, B. J. Roth, and M. Hallett. Optimal focal transcranial magnetic activation of the human motor cortex: effects of coil orientation, shape of the induced current pulse, and stimulus intensity. *Journal of Clinical Neurophysiology*, 9(1):132–136, 1992.

[6] P. C. Miranda, M. de Carvalho, I. Conceição, M. L. Sales Luis, and E. Ducla-Soares. A new method for reproducible coil positioning in transcranial magnetic stimulation mapping. *Electroencephalography and Clinical Neurophysiology*, 105(2):116–123, 1997.

[7] R. J. Ilmoniemi and F. Grandori. A programmable applicator for an electromagnetic field especially for stimulation of the central and peripheral nervous systems and for tissue therapy and hyperthermia applications. FI 100458 B, filed 13$^{\text{th}}$ October, 1993, and issued 15$^{\text{th}}$ December, 1997.

[8] J. Ruohonen and R. J. Ilmoniemi. Multichannel magnetic stimulation: improved stimulus targeting. *Advances in Occupational Medicine and Rehabilitation*, 2(2):55–64, 1996.

[9] J. P. Webb and B. Forghani. T-ω method using hierarchal edge elements. *IEE Proceedings-Science, Measurement and Technology*, 142(2):133–141, 1995.

[10] Z.-D. Deng, S. H. Lisanby, and A. V. Peterchev. Electric field depth–focality tradeoff in transcranial magnetic stimulation: Simulation comparison of 50 coil designs. *Brain Stimulation*, 6(1):1–13, 2013.

[11] N. De Geeter, G. Crevecoeur, and L. Dupré. An efficient 3-D eddy-current solver using an independent impedance method for transcranial magnetic stimulation. *IEEE Transactions on Biomedical Engineering*, 58(2):310–320, 2011.

[12] N. De Geeter, G. Crevecoeur, and L. Dupré. Eddy-current simulations using an independent impedance method in anisotropic biological tissues. *IEEE Transactions on Magnetics*, 47(10):3845–3848, 2011.

[13] N. M. Branston and P. S. Tofts. Analysis of the distribution of currents induced by a changing magnetic field in a volume conductor. *Physics in Medicine and Biology*, 36(2):161–168, 1991.

[14] H. Eaton. Electric field induced in a spherical volume conductor from arbitrary coils: application to magnetic stimulation and MEG. *Medical and Biological Engineering and Computing*, 30(4):433–440, 1992.

[15] D. Geselowitz. On the magnetic field generated outside an inhomogeneous volume conductor by internal current sources. *IEEE Transactions on Magnetics*, 6(2):346–347, 1970.

[16] M. S. Hämäläinen and J. Sarvas. Realistic conductivity geometry model of the human head for interpretation of neuromagnetic data. *IEEE Transactions on Biomedical Engineering*, 36(2):165–171, 1989.

[17] C.-H. Im and C. Lee. Computer-aided performance evaluation of a multichannel transcranial magnetic stimulation system. *IEEE Transactions on Magnetics*, 42(12):3803–3808, 2006.

[18] R. J. Ilmoniemi, M. S. Hämäläinen, and J. Knuutila. The forward and inverse problems in the spherical model. *Biomagnetism: Applications and Theory, edited by Harold Weinberg, Gerhard Stroink, and Timo Katila, Pergamon Press, New York*, 1985.

[19] R. J. Ilmoniemi. The triangle phantom in magnetoencephalography. *The Journal of Japan Biomagnetism and Bioelectromagnetics Society*, 22(1):44–45, 2009.

[20] F. W. Grover. *Inductance Calculations, Working Formulas and Tables*. Van Nostrand Reinhold, 1946.

[21] L. M. Koponen. Practical limitations of TMS-coil focality. Special assignment in the Degree Programme in Engineering Physics and Mathematics, Aalto University, April 2012.

[22] L. M. Koponen, J. O. Nieminen, and R. J. Ilmoniemi. Minimum-energy coils for transcranial magnetic stimulation: application to focal stimulation. In preparation.

[23] L. Heller and D. B. van Hulsteyn. Brain stimulation using electromagnetic sources: theoretical aspects. *Biophysical Journal*, 63(1):129–138, 1992.

[24] J. Nenonen, S. Taulu, M. Kajola, and A. Ahonen. Total information extracted from MEG measurements. In *International Congress Series, New Frontiers in Biomagnetism: Proceedings of the 15th International Conference on Biomagnetism*, volume 1300, pages 245–248, 2007.

[25] A. N. Tikhonov. On the stability of inverse problems. *Doklady Akademii Nauk SSSR*, 39(5):195–198, 1943.

[26] A. L. Hodgkin and A. F. Huxley. A quantitative description of membrane current and its application to conduction and excitation in nerve. *The Journal of Physiology*, 117(4):500–544, 1952.

[27] E. M. Wassermann, C. M. Epstein, U. Ziemann, W. Vincent, P. Tomáš, and S. H. Lisanby. *The Oxford Handbook of Transcranial Stimulation*. Oxford University Press, 2008.

[28] A. V. Peterchev, R. Jalinous, and S. H. Lisanby. A transcranial magnetic stimulator inducing near-rectangular pulses with controllable pulse width (cTMS). *IEEE Transactions on Biomedical Engineering*, 55(1):257–266, 2008.

[29] A. V. Peterchev, D. L. Murphy, and S. H. Lisanby. Repetitive transcranial magnetic stimulator with controllable pulse parameters. *Journal of Neural Engineering*, 8(3):2922–2926, 2011.

[30] A. V. Peterchev. Circuit topology comparison and design analysis for controllable pulse parameter transcranial magnetic stimulators. In *5th International IEEE/EMBS Conference on Neural Engineering (NER)*, pages 646–649, 2011.

[31] S. M. Goetz, M. Pfaeffl, J. Huber, M. Singer, R. Marquardt, and T. Weyh. Circuit topology and control principle for a first magnetic stimulator with fully controllable waveform. In *34th Annual International Conference of the IEEE Engineering in Medicine and Biology Society (EMBC)*, pages 4700–4703, 2012.

[32] S. Bernet, R. Teichmann, A. Zuckerberger, and P. K. Steimer. Comparison of high power IGBTs and hard driven GTOs for high power inverters. *IEEE Transactions on Industry Applications*, 35(2):487–495, 1999.

[33] ABB Semiconductors. `http://www.abb.com/semiconductors/`. Accessed on 30$^{\text{th}}$ April, 2013.

[34] B. H. Han, I. K. Chun, S. C. Lee, and S. Y. Lee. Multichannel magnetic stimulation system design considering mutual couplings among the stimulation coils. *IEEE Transactions on Biomedical Engineering*, 51(5):812–817, 2004.

[35] J. Ruohonen and R. J. Ilmoniemi. Focusing and targeting of magnetic brain stimulation using multiple coils. *Medical and Biological Engineering and Computing*, 36(3):297–301, 1998.

[36] H. H. Rosenbrock. An automatic method for finding the greatest or least value of a function. *The Computer Journal*, 3(3):175–184, 1960.

[37] J. Ruohonen, P. Ravazzani, F. Grandori, and R. J. Ilmoniemi. Theory of multichannel magnetic stimulation: toward functional neuromuscular rehabilitation. *IEEE Transactions on Biomedical Engineering*, 46(6):646–651, 1999.

[38] R. Jiang, B. H. Jansen, B. R. Sheth, and J. Chen. Dynamic multi-channel TMS with reconfigurable coil. *IEEE Transactions on Neural Systems and Rehabilitation Engineering*, 21(3):370–375, 2013.

[39] J. Ruohonen, J. Virtanen, and R. J. Ilmoniemi. Coil optimization for magnetic brain stimulation. *Annals of Biomedical Engineering*, 25(5):840–849, 1997.

[40] G. Xu, Y. Chen, S. Yang, M. Wang, and W. Yan. The optimal design of magnetic coil in transcranial magnetic stimulation. In *27th Annual International Conference of the IEEE Engineering in Medicine and Biology Society*, pages 6221–6224, 2005.

[41] S. L. Ho, G. Xu, W. N. Fu, Q. Yang, H. Hou, and W. Yan. Optimization of array magnetic coil design for functional magnetic stimulation based on improved genetic algorithm. *IEEE Transactions on Magnetics*, 45(10):4849–4852, 2009.

[42] R. C. Trendler. The 10 millisecond 150 kiloampere pulsed power supply for the Fermilab neutrino focussing horn. *IEEE Transactions on Nuclear Science*, 26(3):3977–3979, 1979.

[43] M. B. Schneider and D. J. Mishelevich. Robotic apparatus for targeting and producing deep, focused transcranial magnetic stimulation. US Patent 7,520,848, filed 9$^{\text{th}}$ April, 2004, and issued 21$^{\text{st}}$ April, 2009.

[44] M. B. Schneider and D. J. Mishelevich. Transcranial magnet stimulation of deep brain targets. US Patent Application 12/324,227, filed 26$^{\text{th}}$ November, 2008.

[45] M. B. Schneider and D. J. Mishelevich. Transcranial magnetic stimulation field shaping. US Patent Application 12/838,299, filed 11$^{\text{th}}$ November, 2010.

[46] R. Storn and K. Price. Differential evolution – a simple and efficient heuristic for global optimization over continuous spaces. *Journal of Global Optimization*, 11(4):341–359, 1997.

[47] S. Das, A. Konar, and U. K. Chakraborty. Two improved differential evolution schemes for faster global search. In *Proceedings of the 2005 Conference on Genetic and Evolutionary Computation*, pages 991–998, 2005.

[48] W. H. Lawton and E. A. Sylvestre. Self modeling curve resolution. *Technometrics*, 13(3):617–633, 1971.

[49] P. Paatero and U. Tapper. Positive matrix factorization: a non-negative factor model with optimal utilization of error estimates of data values. *Environmetrics*, 5(2):111–126, 1994.

[50] D. D. Lee and H. S. Seung. Learning the parts of objects by non-negative matrix factorization. *Nature*, 401(6755):788–791, 1999.

[51] C. Ding, T. Li, and M. I. Jordan. Convex and semi-nonnegative matrix factorizations. *IEEE Transactions on Pattern Analysis and Machine Intelligence*, 32(1):45–55, 2010.

[52] G. F. Harpur and R. W. Prager. Development of low entropy coding in a recurrent network. *Network: Computation in Neural Systems*, 7(2):277–284, 1996.

[53] B. A. Olshausen and J. D. Field. Emergence of simple-cell receptive field properties by learning a sparse code for natural images. *Nature*, 381(6583):607–609, 1996.

[54] P. O. Hoyer. Non-negative matrix factorization with sparseness constraints. *The Journal of Machine Learning Research*, 5:1457–1469, 2004.

[55] R. J. Ilmoniemi, J. Ruohonen, and J. Karhu. Transcranial magnetic stimulation — a new tool for functional imaging of the brain. *Critical Reviews in Biomedical Engineering*, 27(3–5):241–284, 1999.

[56] A. Thielscher and T. Kammer. Electric field properties of two commercial figure-8 coils in TMS: calculation of focality and efficiency. *Clinical Neurophysiology*, 115(7):1697–1708, 2004.

[57] M. Nishida, M. Yamaguchi, M. Todo, T. Takayama, H.-Å. Häggblad, and P. Jonsén. Evaluation of dynamic compressive properties of PLA polymer blends using split Hopkinson pressure bar. In *DYMAT 2009-9th International Conference on the Mechanical and Physical Behaviour of Materials under Dynamic Loading*, volume 1, pages 909–915, 2009.

[58] G. N. Peeren. Stream function approach for determining optimal surface currents. *Journal of Computational Physics*, 191(1):305–321, 2003.

[59] Department of Defense Human Factors Engineering Technical Advisory Group. Human engineering design data digest. 2000.

[60] J. O. Nieminen, L. M. Koponen, and R. J. Ilmoniemi. An automatic, computer-controlled TMS-coil calibrator. In *5th International Conference on Non-Invasive Brain Stimulation*, page 305, 2013.

[61] K. H. Mess, P. Schmüser, and S. Wolff. *Superconducting Accelerator Magnets*. World Scientific Publishing Company Incorporated, 1996.

[62] C. B. Eom, M. K. Lee, J. H. Choi, L. J. Belenky, X. Song, et al. High critical current density and enhanced irreversibility field in superconducting MgB_2 thin films. *Nature*, 411(6837):558–560, 2001.

[63] Oxford Instruments. `http://www.oxford-instruments.com/`. Accessed on 30$^{\text{th}}$ April, 2013.

[64] D. Pinchon and P. E. Hoggan. Rotation matrices for real spherical harmonics: general rotations of atomic orbitals in space-fixed axes. *Journal of Physics A: Mathematical and Theoretical*, 40(7):1597, 2007.